Variational Quantum Eigensolvers Applied to Problems in High Energy Physics

by

Ryan Ferguson

A thesis
presented to the University of Waterloo
in fulfillment of the
thesis requirement for the degree of
Master of Science
in
Physics (Quantum Information)

Waterloo, Ontario, Canada, 2021

Author's Declaration

This thesis consists of material all of which I authored or co-authored: see Statement of Contributions included in the thesis. This is a true copy of the thesis, including any required final revisions, as accepted by my examiners.

I understand that my thesis may be made electronically available to the public.

Statement of Contributions

This thesis consists of two manuscripts written for publication. Exceptions to sole authorship of material are as follows:

Research presented in Chapter 2:

Jinglei Zhang, Stefan Kühn, Chris Wilson, Karl Jansen, and Chrsitine Muschik were co-investigators on this project and are co-authors on any future publications relating to this work.

This research was conducted at the University of Waterloo by Ryan Ferguson under the supervision of Jinglei Zhang, Christine Muschik, Karl Jansen, and Stefan Kühn. Ryan Ferguson and Jinglei Zhang individually coded the VQE program for the model. Ryan Ferguson derived the jump formula and the ground state properties of the theory. All MPS calculations were done by Stefan Kühn and all data from Figs. 2.8 and F.1 was collected by Ryan Ferguson. Ryan Ferguson designed Figs. 2.1, 2.8, and F.1, Stefan Kühn designed Figs. 2.2, 2.3, 2.4, and 2.5, and Jinglei Zhang designed Figs. 2.6 and 2.7. Ryan Ferguson wrote the original draft manuscripts, which all co-authors contributed intellectual input on and directly edited. We intend to publish a modified version of this chapter in the near future.

Research presented in Chapter 3:

Luca Dellantonio, Karl Jansen, Abdulrahim Al Balushi, Wolfgang Dür, and Chrsitine Muschik were co-investigators on this project and are co-authors on any publications relating to this work.

This research was conducted at the University of Waterloo by Ryan Ferguson under the supervision of Luca Dellantonio, Christine Muschik, and Wolfgang Dür. Ryan Ferguson and Abdulrahim Al Balushi individually coded the simulation of the measurement-based computations. Ryan Ferguson coded the efficient classical simulation of Pauli measurements and the efficient conversion between stabilizer states and graph states. Ryan Ferguson produced the data in Fig. 3.6 and Abdulrahim Al Balushi produced the data in Fig. 3.7. Ryan Ferguson determined the graph state corresponding to the 2×2 toric code and the graph states corresponding to edge decoration and a layer in the Schwinger circuit after the Pauli measurements were performed classically. The graphic design of all figures was

done by Luca Dellantonio. Ryan Ferguson wrote the original draft manuscripts, which all co-authors contributed intellectual input on and directly edited.

Citations:

Ferguson R R, Dellantonio L, Jansen K, Al Balushi A, Dür W, Muschik C. A measurement-based variational quantum eigensolver. arXiv preprint, arXiv:2010.13940 (2020).

Abstract

Variational methods have long been used to study strongly-correlated quantum systems. Despite the successes of classical protocols, these are limited in the study of quantum systems, either due to numerical errors like the sign problem or the massive memory requirement to represent large quantum systems. Variational quantum eigensolvers (VQEs) overcome these problems and as a result have been an exciting area of research for the past decade. VQEs use a hybrid classical-quantum set-up, where a cost function (usually the expectation value of an operator) is produced by the quantum processor and then optimized on a classical computer. VQEs have been applied to fields such as quantum chemistry, condensed matter physics, high-energy physics, and classical optimization problems. In this thesis, we investigate VQEs to study gauge theories, which describe fundamental physical interactions and are hard to simulate classically. We use two different approaches in implementing a VQE to study two classes of problems.

In the first half of the thesis, we design a VQE to study the $U(1)$ Higgs gauge theory in one spatial dimension. This model is particularly interesting due to the presence of a topological term, which is a candidate to explain the observed CP violation in the universe. In order to perform a quantum simulation of the $U(1)$ Higgs model, the theory is cast on a lattice. In the limit where the lattice size is large and the lattice spacing is small, the continuum limit can be reached and the results correctly resemble the original theory. However, when the lattice is too small or the spacing too big, results are spoiled by finite-size effects. In this thesis, we investigate the effects of a finite lattice and determine the parameters to correctly reproduce a first-order phase transition of the continuous theory. Importantly, to resemble a realistic experiment, we include the statistical and intrinsic quantum noise in our VQE. We design the protocol to be applied on a microwave-photonic platform, which is well-suited due to the bosonic nature of the theory's electrical modes.

In the second half of the thesis, we design a new class of VQEs, based on a measurement-based quantum computer (MBQC) instead of the typical circuit-based set-up. Rather than performing gates on an initial state, a MBQC transforms an initial state by entangling it with a number of auxiliary qubits which are subsequently measured, resulting in a modification of the initial state. In this part of the thesis, we compare the standard, circuit-based VQE with our newly-designed measurement-based VQE (MB-VQE) through two meaningful examples. First, we introduce a novel way to construct variational state families, using measurement-based techniques, that is more costly to access with circuit-based VQEs. We apply this technique to find the ground state of a two-dimensional, periodic Z_2 matter-free lattice gauge theory. In the second approach, we directly translate the circuit-based VQE to a MB-VQE and apply this to the $U(1)$ Schwinger lattice gauge

theory, which is used as a benchmarking problem for VQEs. These examples demonstrate that there are specific problems which are better suited for a MB-VQE.

Acknowledgements

The two years spent completing my master's program have been a fun, but sometimes challenging, time in my life. I am incredible thankful to have had a wonderful supervisor, knowledgeable colleagues, insightful collaborators, and loving, supportive friends and family.

First, I would like to thank my supervisor, Christine Muschik, for giving me the opportunity to work on such interesting projects with many incredibly talented, friendly people. Her insightful guidance and kind demeanor made her the perfect mentor for my journey into the world of quantum simulations and I owe much of my success on these projects to her close supervision. I am incredibly lucky to have worked with her and learned from her on these projects.

With that being said, the completion of these projects and my journey as a master's student is in large part to the excellent research team that I work with, particularly Jinglei Zhang and Luca Dellantonio. They offered invaluable guidance at every step of my journey and were incredibly patient and understand on top of that. They made working on the projects much more enjoyable. Additionally, I would like to thank Abdulrahim Al Balushi, Jan Haase, Amin Jahanpour, Yasar Atas, Angus Kan, and Danny Paulson; they all were very helpful when I had questions and were very fun to work with.

Next, I would like to thank all the superb collaborators I worked with over the course of my studies and the immeasurable help they gave to me. Karl Jansen and Stefan Kühn graciously offered their vast knowledge of high energy physics and lattice gauge theories to the Higgs model simulation project; my research would not be possible without them and I am incredibly grateful to have worked with them. Wolfgang Dür used his incredible expertise in the field of measurement-based quantum computing to make the measurement-based simulation project possible; it was a pleasure and an honour working with him. I would also like to thank Chris Wilson for assisting me with the experimental aspect of the Higgs model simulation project; he offered great insight and helped expand my knowledge.

Finally, I am incredibly thankful for my amazing friends and family, particularly my parents Liz and Rob Ferguson. Allowing me to go away to university was tough on them but they supported me through it all the way. They have made me who I am today and I will always love them. I would also like to thank Anna Gasparini, Jim Gasparini, Christian Gasparini, Joy Ferguson, Wayne Cordes, Elizabeth Worley, Colin Brown, Robyn Cordes, and Sean Cordes for all the love and support, and Leah Varga, Arawn Varga, Caelum Massie, Michael Chisholm, Danella Olsen, Aryeh Fortinsky, Nioka Payne, Nikki Douglas, Jade Colthirst, Lucy Black, Amber Cloves, Aimee Cloves, Sarah Slim, and Alex Vanriel for all their encouragement and the fun times we had together.

Dedication

This is dedicated to Liz Ferguson, Bob Ferguson, Amelia Ferguson, Judy Cordes, Indy, Kirby, Neo, and Luey.

Table of Contents

List of Tables

List of Figures

Chapter 1

Introduction

The field of quantum computing has been one of the most exciting areas of physics in the past few decades. Physicists theorize many areas where quantum computers can be advantageous compared to their classical counterparts, and the fast development of quantum hardware in recent years is bringing practical implementations closer and closer. One of the most interesting advantages of quantum computers is their ability to simulate complex quantum systems. Though classical computers have been extremely successful in studying the physics of strongly correlated quantum systems [1, 2, 3, 4], several barriers pose fundamental obstacles for investigating larger, more complex systems. For example, the infamous sign problem in Markov Chain Monte Carlo simulations generates large numerical errors [5, 6] and the memory needed to store the information on the quantum system grows exponentially with the system's size. These, and other limitations, severely bound the classes of quantum systems that classical computers can simulate.

Though there are many protocols for performing quantum simulations, one of the most promising is the variational quantum eigensolver (VQE) [7, 8, 9]. A VQE consists of a closed feedback loop between a quantum processor and a classical computer. The classical computer provides optimized variational parameters that serve as input for the quantum processor to create a quantum state. A cost function - typically the expectation value of some operator - is efficiently computed on the quantum hardware and then fed back to the classical computer, which uses an optimization algorithm to update the variational parameters. The VQE provides an approximation to the low-lying eigenvalues of the operator, along with the corresponding eigenstates. See Appendix A for an in-depth description of how VQEs work. VQEs have been successfully used in fields such as quantum chemistry [10, 11, 12], high-energy physics [13, 14, 15, 16, 17, 18], and classical optimization. [19, 20].

In this thesis, we apply VQE algorithms to gauge theories. Gauge theories describe the fundamental physical interactions of the universe and, for the reasons mentioned previously, pose a severe challenge to classical simulator. We propose two kinds of VQEs, which we apply to different scenarios. In the first, we consider the U(1) Higgs gauge theory in one spatial dimension with a topological term [21]. Topological terms represent a viable option to explain the CP violation in the universe [22] and can give the theory a rich and interesting phase diagram [5, 23]. To obtain the Hamiltonian formulation of the theory, we first cast the model on a lattice. We then simulate a VQE including statistical noise to determine the ground states of the theory for different parameter regimes and to explore the phase structure of the model. In the second scenario, we outline the protocol of a new kind of VQE where the quantum resource is a measurement-based quantum computer (MBQC) [24, 25, 26, 27, 28, 29] instead of a circuit. In this case, rather than applying gates on an initial state, a highly entangled state is first prepared, and the output qubits are modified by local measurements on auxiliary qubits. These qubits are measured in bases controlled by the variational parameters, which are optimized by the classical algorithm. We consider two different approaches to implement measurement-based VQEs (MB-VQEs), and apply them to relevant problems: a two-dimensional periodic Z_2 matter-free lattice gauge theory [30] and the U(1) Schwinger lattice gauge theory in one spatial dimension [31]. Both of these examples showcase situations where MB-VQEs are better suited than circuit-based VQEs.

The thesis is structured as follows. In Chapter 2, we investigate the U(1) Higgs lattice gauge theory and simulate a VQE to find its ground state in different parameter regimes. First, we derive the Hamiltonian of the model and discuss the dynamical contributions from the inclusion of a topological term. In particular, we study the phase diagram of the model along with the first-order phase transition induced by the topological term. We use truncated operators along with matrix product states (MPS) [32, 33, 34] to investigate these effects. Then, we discuss the advantages of performing the VQE on a microwave photon platform. Finally, we simulate the VQE with statistical noise and observe the phase transition.

In Chapter 3 we introduce MB-VQEs and compare them to circuit-based VQEs. First, we summarize the relevant features of MBQCs, including their ability to perform all the Clifford operations in a single step at the beginning of the procedure [27]. Then, we introduce a novel way to construct variational state families using measurement-based techniques, that is more costly to access with circuit-based VQEs. This is applied to find the ground state of a two-dimensional, periodic Z_2 matter-free lattice gauge theory, which is equivalent to the toric code Hamiltonian with a perturbation [30]. Finally, we directly translate a circuit-based VQE into a MB-VQE, in the process effectively removing all the

Clifford operations from the MB-VQE. This is used to simulate the ground state of the U(1) Schwinger lattice gauge theory in one spatial dimension.

Chapter 2

A Microwave-Based VQE for Simulating Topological Terms

2.1 Introduction

Although classical simulations of lattice gauge theories have resulted in important break-throughs [35, 36], major issues like the sign problem greatly reduce their effectiveness in studying quantum problems [37, 38]. The sign problem arises when topological terms are present [5, 6], which play an important and fascinating role in quantum field theory. They induce CP violation, and in QCD this leads to the possibility to explain the strong CP problem [39] and shed light on physics beyond the standard model [40]. In a gauge Higgs theory, CP violation is one of the basic ingredients for generating the matter-antimatter asymmetry of the universe [22] (see Fig. 2.1). In 1+1 dimensions, the strength of the topological term is given by the parameter θ, the presence of which can lead to new phases and therefore to an enriched phase structure of the model (see [5, 23] for a discussion of the effect of such θ-terms in various dimensions).

One classical method that can overcome some of these difficulties are tensor networks, which have been very successful in simulating one dimensional gauge theories [41, 42]. Although it is challenging to extend them to two dimensions, some methods have been already proposed [43]. Another promising alternative to Markov Chain Monte Carlo (MCMC) calculations are quantum simulations, which are not affected by the sign problem and thus offer exciting opportunities to study topological terms in one or more spatial dimensions. Currently, quantum simulations have been used in proof-of-principle simulations of lattice gauge theories without topological terms in one spatial dimension [16, 44], but in the fu-

ture, simulations in three spatial dimensions will allow us to explore the open questions in high energy physics (see Refs. [14, 15] for progress in this direction).

In this chapter, we use a quantum simulation to determine the ground state properties of a lattice gauge theory in one spatial dimension with a topological term. In particular, we study the U(1) Abelian Higgs lattice gauge theory with a semiclassical approximation with a topological term and open boundary conditions [21, 45, 46]. The rich physics content found in this model cannot be explored with conventional MCMC lattice methods because the topological term induces a sign problem in Euclidean time. However, it has been realized that in the special case of 1+1 dimensions the model can be written in a dual formulation which is sign problem free [47]. Going, as targeted here, to 1+1 dimensions, a gauge-Higgs model with a topological term is also closely related to models in condensed matter physics [6, 48, 49].

In the following we focus on the phase diagram of the model in one spatial dimension. As shown in Fig. 2.1, the physics of the model is periodic in θ and, as will be discussed more in detail below, in the confining region (for large masses of the Higgs field) the ground state undergoes a first-order phase transition for varying θ that manifests as a sharp discontinuity of the electric field density of the state. On the other hand, in the Higgs region (for small masses of the Higgs field) there will be no dependence of the electric field density on θ. Therefore, there are two distinct phases that we can identify by studying the ground state properties for a variety of parameters of the model. We first explore the physics of the model in the Hamiltonian formalism using matrix product states (MPS) [32, 33, 34]. This allows us to diagonalize the Hamiltonian on lattices of various sizes and various truncations of the Higgs field's Hilbert space. We find that, despite the finite lattice size and truncated operators, we are able to capture the physics of the main features of the phase diagram from analytic results and we can simulate it using currently available quantum platforms.

A particularly suitable quantum simulation method for this purpose is a variational quantum eigensolver (VQE) [7, 8, 9]. This algorithm takes advantage of a quantum processor to efficiently generate a parameterized ansatz state. An appropriate cost function is measured on the state and fed into a classical processor. The classical processor uses this information to minimize the cost function by optimizing the parameters that control the ansatz state. VQEs exploit the quantum processor to efficiently evaluate the cost function that is hard to calculate classically, while the variational nature of the optimization algorithm ensures resilience to certain types of errors and lowers requirements for the quantum hardware. The VQE algorithm is explained in more detail in Appendix A.

We propose an experimental VQE realization using superconducting microwave cavities (see Fig. 2.1). As we discuss below, this experimental platform is well-suited for our
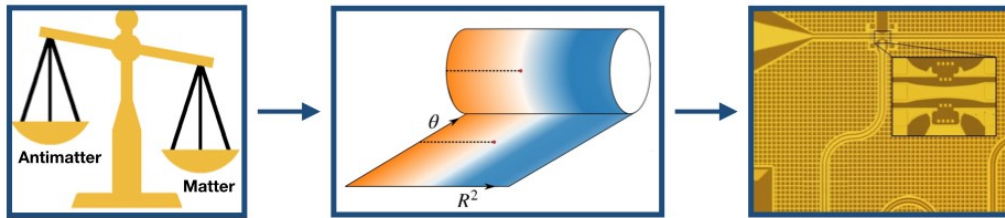
Figure 2.1: **Conceptual overview of Chapter 2**. *Left:* Topological terms are play an important role in quantum field theory: among other effects, they have been considered as a possible explanation of the matter-antimatter imbalance observed in the universe. However their physics is difficult to study with classical numerical methods since it is affected by the sign problem. *Center:* When a topological term θ is introduced to the U(1) Higgs lattice gauge theory in 1D, its phase diagram becomes periodic in θ and develops a first-order symmetry-breaking phase transition (dashed line) which only occurs for small R^2 (large masses of the Higgs field). This is discussed more in depth in Section 2.3. *Right:* To perform a VQE of the Higgs model with a topological term and simulate its phase diagram, a microwave-photon cavity is our platform of choice. See Sections 2.5 and 2.6 for more details. Image of the experimental platform is adapted with permission from Ref. [50].

problem and has promising features that motivated us in pioneering its application for quantum simulations. The bosonic nature of microwave photons makes them apt to model the bosonic Higgs fields' degrees of freedom: this allows to better exploit the available experimental modes. Furthermore, in superconducting microwave cavities Josephson junctions are an important source of strong nonlinear dynamics: through parametric processes it is possible to easily select and enhance particular interactions between the cavity modes. This flexibility in the available interactions is an important resource in a VQE, since they determine the form of the ansatz state and are fundamental in the success of the algorithm.

The rest of the chapter is organized as follows. In Section 2.2 we briefly introduce the model with a particular focus on the Hamiltonian lattice formulation. We summarize the main features of the phase structure in Section 2.3. Subsequently we numerically demonstrate, using MPS, that we can capture the relevant physics of the model, even for system sizes available on current quantum hardware, and we systematically explore finite size effects in Section 2.4. In Section 2.5 we describe the experimental resources relevant for our simulation algorithm and in Section 2.6 we discuss in detail the VQE protocol and the key results. We summarize our findings and offer some possible perspectives in Section 2.7.

2.2 The U(1) Higgs Model with a Topological Term

Contrary to conventional lattice methods, for the purpose of quantum simulations it is advantageous to work with a Hamiltonian lattice formulation. Hence, we describe here the U(1) Higgs lattice Hamiltonian with a topological term in one spatial dimension with open boundary conditions. In Section 2.2.1 we introduce the Hamiltonian of the model, which involves both scalar Higgs and gauge fields, and we give the Gauss Law, which is the conservation law that enforces local gauge invariance. In Section 2.2.2 we derive an effective Hamiltonian in which gauge degrees of freedom are integrated out, such that the Hamiltonian depends only on the Higgs field operators.

2.2.1 The Hamiltonian

Here we introduce the U(1) Higgs lattice model in one spatial dimension. The Higgs fields are defined on the lattice sites and the gauge fields are defined on the links between the lattice sites. In particular, the Higgs field on lattice site n is $\hat{\phi}_n$ and it has a canonically conjugate operator $\hat{Q}_n$, called the charge operator. By fixing the length of the Higgs field (see Appendix B for details), these operators satisfy the commutation relation [21, 45, 46]

$$[\hat{Q}_n, \hat{\phi}_{n'}^\dagger] = \delta_{n,n'} \hat{\phi}_n^\dagger, \tag{2.1}$$

and as a result the Higgs field $\hat{\phi}_n$ acts as a descending operator for the eigenstates of $\hat{Q}_n$:

$$\hat{Q}_n |Q\rangle_n = Q|Q\rangle_n, \quad Q \in \mathbb{Z}, \tag{2.2a}$$

$$\hat{\phi}_n |Q\rangle_n = |Q-1\rangle_n. \tag{2.2b}$$

The operator $\hat{U}_n$ is associated with the gauge field on link n, which joins lattice sites n and $n+1$, and it has a canonically conjugate operator $\hat{E}_n$, called the electric field operator. These operators satisfy the commutation relation [21, 45, 46]

$$[\hat{E}_n, \hat{U}_{n'}^\dagger] = \delta_{n,n'} \hat{U}_n^\dagger, \tag{2.3}$$

and $\hat{U}_n$ is a descending operator for the eigenstates of the electric field $\hat{E}_n$:

$$\hat{E}_n |E\rangle_n = E|E\rangle_n \quad E \in \mathbb{Z}, \tag{2.4a}$$

$$\hat{U}_n |E\rangle_n = |E-1\rangle_n. \tag{2.4b}$$

The U(1) Higgs Hamiltonian for one spatial dimension is given by [21]

$$\hat{H} = \frac{1}{2R^2} \sum_{n=1}^{N} \hat{Q}_n^2 - \frac{R^2}{2} \sum_{n=1}^{N-1} \left(\hat{\phi}_n^\dagger \hat{U}_n^\dagger \hat{\phi}_{n+1} + \text{H.C.} \right)$$
$$+ \frac{1}{2\beta} \sum_{n=1}^{N-1} \left(\varepsilon_0 + \hat{E}_n \right)^2 - \beta(N-1), \tag{2.5}$$

where N is the number of lattice sites, $\beta = 1/g^2$ where g is the coupling strength, and R^2 is inversely proportional to the mass of the Higgs field. Additionally, ε_0 is the background electric field. In one spatial dimension, the topological term is proportional to the background electric field $\theta = 2\pi\varepsilon_0$ [51]. In Eq. (2.5) we have fixed the lattice spacing to be $a = 1$ and use natural units $\hbar = c = 1$. The first and third term in the Hamiltonian describe the Higgs field energy and electric field energy respectively. The second term is referred to as the kinetic term; it allows charge to be transferred between adjacent lattice sites, at the expense of changing the electric field between the sites. The presence of the gauge field operator in this term ensures the local gauge symmetries of the model are conserved.

In the Hamiltonian formulation of the model, physical states (*i.e.* gauge-invariant states) have to obey the Gauss Law

$$\hat{G}_n |\Psi_{\text{physical}}\rangle = G_n |\Psi_{\text{physical}}\rangle, \tag{2.6}$$

where we have defined for each lattice site

$$\hat{G}_n = \hat{E}_n - \hat{E}_{n-1} - \hat{Q}_n. \tag{2.7}$$

Note that the $\hat{G}_n$ operators commute with the Hamiltonian and are the generators of the local gauge transformations associated with the theory. The eigenvalues G_n take integer values and can be interpreted as static charges that can be introduced at every lattice site. For the rest of this chapter we focus on the sector of vanishing external charges, $G_n = 0$ $\forall n$.

The Hamiltonian in Eq. (2.5) conserves the total charge

$$\hat{Q}_{\text{total}} = \sum_{n=1}^{N} \hat{Q}_n. \tag{2.8}$$

As a result, the Hilbert space can be divided into subsectors defined by the total charge of the states within. For the remainder of the chapter we will focus on the ground state

properties of the theory in the $Q_{\text{total}} = 0$ subsector. In order to ensure that the ground state is in the correct subsector during numerical calculations, we add a penalty term to the Hamiltonian

$$\hat{H}_{\text{penalty}} = \ell \left(\sum_{n=1}^{N} \hat{Q}_n \right)^2 . \tag{2.9}$$

When the weight ℓ of this term is large enough, it ensures that the states outside of the $Q_{\text{total}} = 0$ sector are penalized and removed from the low-lying spectrum.

2.2.2 Elimination of the Gauge Fields

In the following, we express the Hamiltonian in Eq. (2.5) in terms of Higgs degrees of freedom only. Eliminating the gauge degrees of freedom [52, 53, 54, 55] ensures that the eigenstates of the effective Hamiltonian are gauge invariant, and therefore allows for a contained quantum simulation, that takes place only in the gauge invariant (physical) subspace.

By considering the subspace of the theory with zero static charge, $\hat{G}_n | \Psi_{\text{physical}} \rangle = 0$, Eq. (2.7) can be rewritten as

$$\hat{E}_n = \hat{E}_{n-1} + \hat{Q}_n \tag{2.10}$$

for the physical states. Using open boundary conditions, Eq. (2.10) can be solved to obtain the electric field at every site to be

$$\hat{E}_n = \sum_{k=1}^{n} \hat{Q}_k. \tag{2.11}$$

Eq. (2.11) allows us to write the electric field operators entirely in terms of the charge operators. In particular, the electric term of the Hamiltonian can be rewritten as

$$\sum_{n=1}^{N-1} \left(\varepsilon_0 + \hat{E}_n \right)^2 = \sum_{n=1}^{N-1} \left(\varepsilon_0 + \sum_{k=1}^{n} \hat{Q}_k \right)^2$$

$$= \sum_{n=1}^{N-1} (N-n) \hat{Q}_n^2 + 2 \sum_{n=2}^{N-1} \sum_{j=1}^{n-1} (N-n) \hat{Q}_j \hat{Q}_n \tag{2.12}$$

$$+ 2\varepsilon_0 \sum_{n=1}^{N-1} (N-n) \hat{Q}_n + (N-1)\varepsilon_0^2$$

9

To eliminate the gauge fields operators $\hat{U}_n$ and $\hat{E}_n$ from Eq. (2.5), we can redefine the Higgs fields $\hat{\phi}_n$ as follows [55]

$$\hat{\phi}_n \to \left(\prod_{k=1}^{n-1} \hat{U}_k^\dagger\right) \hat{\phi}_n,$$

$$\hat{\phi}_n^\dagger \to \hat{\phi}_n^\dagger \left(\prod_{k=1}^{n-1} \hat{U}_{n-k}\right).$$

This induces the transformation

$$\hat{\phi}_n^\dagger \hat{U}_n^\dagger \hat{\phi}_{n+1} \to \hat{\phi}_n^\dagger \hat{\phi}_{n+1}.$$

This transformation, as well as Eq. (2.12), allow us to obtain an effective Hamiltonian where the gauge degrees of freedom have been eliminated

$$
\begin{aligned}
\hat{H} = {}&\frac{1}{2R^2} \sum_{n=1}^{N} \hat{Q}_n^2 - \frac{R^2}{2} \sum_{n=1}^{N-1} \left(\hat{\phi}_n^\dagger \hat{\phi}_{n+1} + \text{H.C.}\right) + \frac{1}{2\beta} \sum_{n=1}^{N-1} (N-n)\hat{Q}_n^2 \\
&+ \frac{1}{\beta} \sum_{n=2}^{N-1} \sum_{j=1}^{n-1} (N-n)\hat{Q}_j \hat{Q}_n + \frac{\varepsilon_0}{\beta} \sum_{n=1}^{N-1} (N-n)\hat{Q}_n - \beta(N-1) + \frac{\varepsilon_0^2}{2\beta}(N-1).
\end{aligned}
\tag{2.14}
$$

As Eq. (2.14) shows, expressing the effective Hamiltonian purely in terms of Higgs field operators $\hat{\phi}_n$ and $\hat{Q}_n$ introduces long-range interactions. It also allows one to simulate the model using fewer modes, as the redundant degrees of freedom have been removed. A method for obtaining the effective Hamiltonian in more than one spatial dimension is described in Refs. [14, 15].

2.3 Phase Structure and Ground State Properties

Despite its simplicity, the U(1) Higgs model shows a rich phase diagram, in particular when a topological term is added to the theory, which makes it especially interesting for quantum simulation. In this section we briefly review the phase structure of the model, before systematically exploring how limitations of current small-scale quantum hardware affect this picture in Section 2.4. We first focus on the case without a topological θ-term in Section 2.3.1 before moving on to the phase structure in the presence of a θ-term in Section 2.3.2. We discuss the signature of detecting a quantum phase transition when ε_0
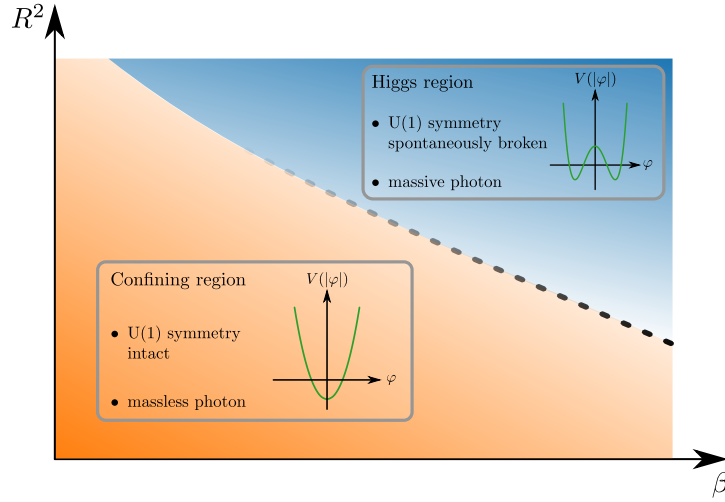
Figure 2.2: **Phase diagram of the Abelian Higgs model with fixed length of the field in the $R^2 - \beta$ plane.** The Higgs region is indicated in blue whereas the confinement region is indicated in orange. The dashed line corresponds to a crossover between the Higgs and the confining region. The insets show a sketch of the form of the potential in the different regions. Note that R^2 is inversely proportional to the mass of the Higgs field. This figure was made by Stefan Kühn.

in Eq. (2.5) is varied and which can be observed in a quantum simulation even for small system sizes. This quantum phase is of particular interest to us, as it is not accessible with conventional MCMC methods due to the sign problem. Hence, we aim to design a microwave based quantum simulation experiment, as we discuss in detail in Section 2.5.

2.3.1 Phase Structure in the Absence of a Topological Term

In the absence of a topological θ-term, the Higgs model with fixed length of the field can be studied numerically with conventional MCMC lattice methods [45, 46, 56]. An intuition for the phase structure can also be obtained by examining the Lagrangian using a simple semiclassical approach (see Appendix B for details). In this picture, the scalar field φ is assumed to fluctuate only slightly around the minimum of the potential term $V(|\varphi|)$ in the Lagrangian for the ground state of the model. Depending on the value of the mass and the coupling, the shape of $V(|\varphi|)$, and consequently the nature of the ground state, changes as shown in Fig. 2.2. For large values of the mass and small inverse coupling, or equivalently small values of R^2 and β, the potential has a unique minimum. In this region,

11

the Abelian Higgs model essentially corresponds to a pure U(1) gauge theory, describing nothing but a massless photon. Since pure gauge theories in their compact version show charge confinement, we refer to this part of phase diagram as the confining region.

Going into the opposite corner of the phase diagram in Fig. 2.2, characterized by small values of the mass and large inverse coupling, the potential $V(|\varphi|)$ shows a "Mexican hat" structure with an infinite number of minima along the well of the Mexican hat. In this region, the photon acquires a mass as a result of the Brout-Englers-Higgs mechanism (see Appendix B for details) and we refer to this part as the Higgs region. The ground state in the Higgs region corresponds to one of the minima of the Mexican hat potential and, thus, spontaneously breaks the U(1) symmetry of the model.

On a lattice with finite spacing, these two regions of the phase diagram are separated by a crossover that is disappearing for small values of the inverse coupling β. Taking the continuum limit, the crossover line ends in a Berezinskii-Kosterlitz-Thouless transition from a confining phase [1] for large masses to the Higgs phase at small values of the mass [56].

2.3.2   Phase Structure in the Presence of a Topological Term

The phase structure of the model in the presence of a topological term has been investigated both theoretically [49] and numerically [57, 58]. Note that the topological term gets its name from QCD, where the theta term depends on the topology of the considered space [59]. Fig. 2.3 shows a sketch of the phase diagram as a function of ε_0 (the background electric field) and R^2 for a fixed value of β.

Most notably, the physics is periodic in ε_0 with period 1. The origin of this periodicity can be understood intuitively by looking at the electric energy in Eq. (2.5). It is always possible to shift the electric field by an integer k, such that $\varepsilon_0' := \varepsilon_0 - k \in [0, 1)$ while the electric energy stays unchanged

$$\sum_{n=1}^{N-1} \left(\varepsilon_0 + \hat{E}_n \right)^2 = \sum_{n=1}^{N-1} \left(\varepsilon_0 - k + \hat{E}_n + k \right)^2 = \sum_{n=1}^{N-1} \left(\varepsilon_0' + \hat{E}_n' \right)^2.$$

The shifted electric field $\hat{E}_n' := \hat{E}_n + k$ has the same spectral properties as $\hat{E}_n$ in Eq. (2.4a) and the resulting configuration fulfills Gauss Law, provided the original one was gauge invariant. Hence, such a shift does not change physics and we can restrict ourselves for

---

[1] Strictly speaking, one should refer to "regions" in the phase diagram, since there is an analytical connection between the different regions in the phase diagram

the following discussion to $\varepsilon_0 \in [0, 1)$. Moreover, the two points $\varepsilon_0 = 0, 1/2$ are special, because for these cases the Hamiltonian is symmetric under charge conjugation, meaning the exchange of particles and antiparticles (rigorous proofs for the periodicity and the charge conjugation symmetry are provided in Appendix C).

To get further insight into the phase diagram in Fig. 2.3, we can examine the Hamiltonian in Eq. (2.5) [or its unitarily equivalent version in Eq. (2.14)] in the limiting cases of large and vanishing mass of the Higgs field. Focusing first on the limit of small mass corresponding to $R^2 \gg 1$, Eq. (2.14) reduces to

$$-\frac{R^2}{2} \sum_{n=1}^{N-1} (\hat{\phi}_n \hat{\phi}_{n+1}^\dagger + \text{H.C.}),$$

which is a pure hopping Hamiltonian. In particular, we see that the expression above is independent of ε_0 and thus the physics does not depend on the topological term. Since we focus on the sector of vanishing total charge, the ground state in this limit is given by a superposition of all zero-total-charge states.

Looking at the opposite limit of large mass, or equivalently $R^2 \ll 1$, the Hamiltonian in Eq. (2.5) reduces to

$$\frac{1}{2R^2} \sum_{n=1}^{N} \hat{Q}_n^2 + \frac{1}{2\beta} \sum_{n=1}^{N-1} \left(\varepsilon_0 + \hat{E}_n \right)^2. \tag{2.15}$$

The first term energetically favors a vanishing charge at every site, $Q_n = 0 \ \forall n$. Plugging this into Gauss Law in Eq. (2.10) and taking into account that we focus on the sector of vanishing external charges, we see that for gauge invariant states the electric field has to take a constant value for all sites. For $\varepsilon_0 < 1/2$ the field configuration minimizing the electric energy in Eq. (2.15) is given by $E_n = 0 \ \forall n$. In contrast, for $\varepsilon_0 > 1/2$ an electric field of $E_n = -1 \ \forall n$ minimizes the energy. Exactly at the point $\varepsilon_0 = 1/2$ both configurations yield the same electric energy contribution, and the ground state is doubly degenerate. These considerations show that in the limit of large masses the model undergoes a first-order quantum phase transition as we increase ε_0 from 0 to 1. This transition is accompanied by a discontinuity in the electric field density (EFD)

$$\begin{aligned} F &= \frac{1}{N-1} \sum_{n=1}^{N-1} \langle \hat{E}_n + \varepsilon_0 \rangle \\ &= \frac{1}{N-1} \sum_{n=1}^{N-1} (N-n) \langle \hat{Q}_n \rangle + \varepsilon_0 \end{aligned} \tag{2.16}$$
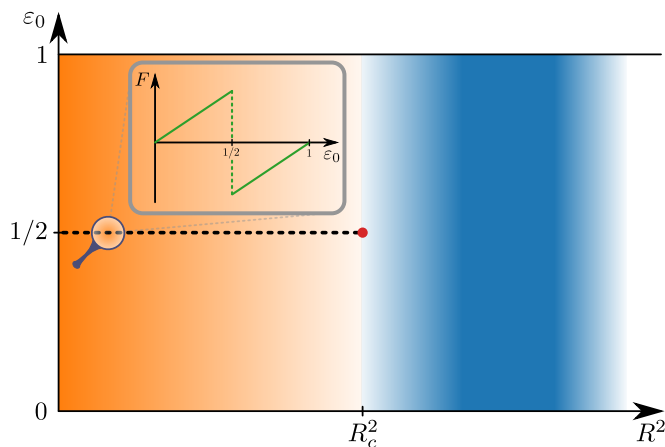
13

Figure 2.3: **Sketch of the phase diagram in the $R^2 - \varepsilon_0$ plane.** The dashed line indicates the critical line corresponding to first-order phase transition which ends in a second-order quantum phase transition (indicated by the red dot). The confining region is indicated in orange, the Higgs region in blue. The inset shows the behavior of the electric field density which, when crossing the phase transition, showing a jump as a result of the first-order transition (see discussion in the main text). This behavior of the electric field density will serve as the signature of the phase transition for the here performed quantum simulation of the model. This figure was made my Stefan Kühn.

which we expect for $R^2 \ll 1$ to behave as

$$
F \approx \begin{cases} \varepsilon_0 & \text{for } \varepsilon_0 \leq 1/2 \\ \varepsilon_0 - 1 & \text{for } \varepsilon_0 > 1/2, \end{cases}
$$

as shown in the inset of Fig. 2.3. Moreover, the abrupt jump in the electric field configuration for $\varepsilon_0 = 1/2$ by one unit leads to a cusp in the electric energy term. Hence, we expect the ground state energy to show a non-smooth behavior at the transition point too. These expectations, which will be verified in Section 2.4, will serve as the signature of the phase transition for the microwave-based quantum simulation of the model we perform.

Our discussion of the two limiting cases shows that the behavior of the model has to change going from large masses (corresponding to small R^2) to small masses (corresponding to large R^2). While for small masses a first-order quantum phase transition occurs for $\varepsilon_0 = 1/2$, this transition vanishes in the limit of large mass. Ref. [49] argued that the critical line at $\varepsilon_0 = 1/2$ ends in a second-order quantum phase transition belonging to the Ising universality class at a critical value R_c^2. This transition is accompanied by a spontaneous

breaking of the charge conjugation symmetry and has been observed in numerical MCMC simulations using a dual lattice formulation of the model [57]. In other words, the charge conjugation symmetry is present in the model for $\varepsilon_0 = 1/2$ and $R^2 < R_c^2$, but not for $\varepsilon_0 = 1/2$ and $R^2 \geq R_c^2$. Moreover, despite the new features arising from the θ-term, the picture from the previous section remains true for large enough values of inverse coupling. For large mass, or equivalently small R^2, there is a confining region whereas for large values of R^2 again the Higgs region occurs (see Fig. 2.3).

In the following we aim to design a microwave-based quantum simulation experiment allowing us to determine the phase structure of the model in the presence of a topological term. Since current quantum hardware is of small-scale, we will to restrict ourselves to a small number of degrees of freedom and we have to work with lattices consisting only of a few sites. It can be shown that even for such a small system the considerations above hold true, but the location of the first phase transition shifts from $\varepsilon_0 = 1/2$ to some larger value of ε_0. Assuming the mass is large enough that the kinetic term can be neglected, we show in Appendix D that the first phase transition occurs at

$$\varepsilon_0 = \frac{1}{2} + \frac{\beta}{R^2(N-1)}. \tag{2.17}$$

Note that the dominant basis state in the ground state before the phase transition is the one with charge configuration $|0\rangle^{\otimes N}$, whereas after the transition the basis state with charge configuration $|-1\rangle|0\rangle^{\otimes N-2}|+1\rangle$ dominates. Equation (2.17) predicts the phase transition cannot occur before $\varepsilon_0 = 1/2$ for a finite lattice and only in the $N \to \infty$ limit, the phase transition occurs exactly at $\varepsilon_0 = 1/2$.

2.4 Spin Truncation and Matrix Product States

Our goal in this chapter is to explore the physics of the model using existing small-scale quantum hardware. To assess the feasibility of such an approach we first explore the effects of truncating the model to a small number of degrees of freedom numerically using matrix product states (MPS). For a system with N sites and open boundary conditions, the MPS ansatz reads

$$|\psi\rangle = \sum_{i_1, i_2, \dots, i_N}^{d} M_1^{i_1} M_2^{i_2} \cdots M_N^{i_N} |i_1\rangle \otimes |i_2\rangle \otimes \cdots \otimes |i_N\rangle.$$

In the expression above, $M_k^{i_k}$ are complex square matrices of size χ for $1 < k < N$, and $M_1^{i_1}$ ($M_N^{i_N}$) is a χ-dimensional row (column) vector. The states $\{|i_k\rangle\}_{i_k=1}^{d}$ are a basis for the d-dimensional local Hilbert space on site k. The parameter χ is called the bond dimension of

the MPS and determines the number of variational parameters in the ansatz and limits the amount of entanglement that can be present in the state (see Refs. [32, 33, 34] for detailed reviews). The optimal set of tensors can be found variationally by iteratively minimizing the energy for each tensor while keeping the others fixed [60].

For numerical calculations with MPS, the dimension of the local Hilbert spaces has to be finite, which is in contrast to the infinite-dimensional degrees of freedom for each site in the Higgs Hamiltonian. Hence, they have to be truncated to a finite dimension. In Section 2.4.1 we discuss a way of truncating the Hilbert spaces before numerically exploring finite-size effects on the phase structure in the presence of a θ-term in Section 2.4.2.

2.4.1   Spin Truncation

One possibility of truncating the theory is to replace the bosonic fields with integer spins

$$\hat{Q}_n \to \hat{S}_n^z, \qquad \hat{\phi}_n^\dagger \to \frac{1}{|S|}\hat{S}_n^+, \tag{2.18}$$

where $\hat{S}^z$ and $\hat{S}^+$ are the z-component and raising operators for a particle with spin s, respectively, and $|S| = \sqrt{s(s+1)}$. The resulting local Hilbert space is finite and has dimension $d = 2s + 1$. Using this mapping, the commutation relations of the original model stay intact (see Section 2.2.1 for more details on the commutation relations) except for

$$[\hat{\phi}_n, \hat{\phi}_{n'}^\dagger] \to \left[\frac{1}{|S|}\hat{S}_n^-, \frac{1}{|S|}\hat{S}_{n'}^+\right] = \frac{2}{|S|^2}\delta_{n,n'}\hat{S}_n^z.$$

Notice that the expression above approaches the correct commutation relation for bosonic field operators, $[\hat{\phi}_n, \hat{\phi}_{n'}^\dagger] = 0$, in the limit $s \to \infty$. The resulting spin Hamiltonian after applying the mapping in Eq. (2.18) to Eq. (2.14) can be addressed with MPS using standard methods, despite its long-range interactions [42, 53, 61, 62, 63].

2.4.2   MPS Results

In order to examine the effects of truncating the model to a small, finite number of degrees of freedom on the phase structure, we study the spin Hamiltonian at fixed coupling strength for a wide range of values of R^2, s, and N. To estimate the error due to the finite size χ of the matrices in our numerical MPS simulations, we repeat the calculation for every combination of (R^2, N, s) for a range of bond dimensions (the size of the truncated matrices

16

$M_k^{i_k}$) $\chi \in [10, 100]$. Afterwards we can extrapolate the results to the limit $\chi \to \infty$ following Ref. [42]. Figure 2.4 shows the MPS results obtained for the ground state energy density E_0/N and the EFD as a function of ε_0 for various system sizes and couplings. For all the results presented, we have chosen a penalty strength of $\ell = 3N$ which is sufficient to ensure that we are in the sector of vanishing total charge.

Figure 2.4: **MPS plots of Higgs phase diagram**. Ground state energy (left column) and EFD (right column) as a function of ε_0 calculated using MPS for $\beta = 1.0$ and $R^2 = 0.3$ (first row), 0.6 (second row) and 1.0 (third row). Dots indicate $s = 1$, triangles $s = 2$ and the different colors encode the different system sizes $N = 4$ (blue), 8 (orange), 20 (green) and 100 (red). As a guide for the eye the markers are connected with lines. The error bars represent the uncertainty from the extrapolation in χ. These plots were made by Stefan Kühn.

In general, we observe that truncation effects due to the finite value of s are rather small, and even the simplest nontrivial truncation, $s = 1$, is sufficient to avoid noticeable effects throughout the range of masses we explore. Only for the smallest mass we study, corresponding to $R^2 = 1.0$, results for $s = 1$ and $s = 2$ start to differ slightly, in particular

for larger values of ε_0. Nevertheless, even in these cases deviations are relatively modest.

In contrast to the spin truncation, finite-size effects are more pronounced. While we expect the physics to be periodic in ε_0 with period 1 as outlined in Section 2.3.2, Fig. 2.4 shows that ground state energy density as well as the EFD only show perfect periodicity throughout the entire range of ε_0 we study for our largest system size, $N = 100$. For smaller values of N the characteristic features still repeat, however the graphs for the energy density and the EFD show an overall increasing trend with ε_0. Moreover, the period at which the characteristic features repeat is increasing with decreasing system size.

Focusing on our results for $R^2 = 0.3$ in Figs. 2.4(a) and 2.4(b), corresponding to the largest value of the mass we consider, we clearly see the signatures of the first-order phase transition as discussed in Section 2.3.2. The EFD shows sharp discontinuities accompanied by cusps in the ground state energy for all system sizes we study. For our largest system size, $N = 100$, these transitions occur for ε_0 close to integer multiples of $1/2$. Decreasing the system size, we observe that the location of the first transition gradually shifts to larger values of ε_0, in agreement with Eq. (2.17). In particular, even for an extremely small system size of $N = 4$ the signatures of phase transition are still clearly visible in both the EFD and the ground state energy density.

Going to a significantly smaller mass, the discontinuities and cusps in the EFD as well as the ground state energy density vanish, as our data for $R^2 = 1.0$ in Figs. 2.4(e) and 2.4(f) reveal. The smooth behavior of these observables is giving a clear indication that we are in the regime below the critical mass, or correspondingly $R^2 > R_c^2$, and the phase transition is gone. In general, finite-size effects seem to shift the critical mass at which the transitions vanishes towards smaller values (or equivalently R_c^2 towards higher values), as our data for $R^2 = 0.6$ reveals. Looking at Figs. 2.4(c) and 2.4(d) we clearly observe a first-order order transition signaled by a sharp discontinuity in the EFD for system sizes $N \geq 20$. In contrast, the discontinuities are no longer present for the two smallest system sizes $N = 4, 8$ we study, and the EFD curves for these cases are smooth.

From our data in Figs. 2.4(a) - 2.4(d) we can extract the location ε_0' of the first-order phase transition as the first discontinuity (cusp) in the EFD (energy density). Fig. 2.5 contains our results for $R^2 = 0.3$, 0.6 and various system sizes. Both panels show that finite-size effects shift the location of the first transition to values $\varepsilon_0' > 1/2$. Comparing our numerical data to the prediction for the large mass limit $R^2 \ll 1$ in Eq. (2.17), we observe good agreement for $R^2 = 0.3$. Going to a larger value of $R^2 = 0.6$, or equivalently to a smaller mass, the approximation in Eq. (2.17) breaks down and is no longer compatible with the numerical data.

In summary, our MPS data demonstrates that we can observe the relevant features
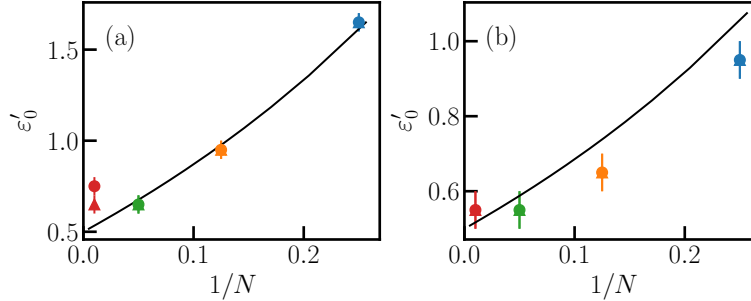
Figure 2.5: **Location of phase transition for finite lattice size.** Location of the first discontinuity extracted from our numerical data as a function of system size for $\beta = 1.0$ and $R^2 = 0.3$ *(a)*, and 0.6 *(b)*. Dots indicate $s = 1$, triangles $s = 2$, and the solid line the prediction from Eq. (2.17) for the large mass limit. The error bars originate from our finite resolution in ε_0. These plots were made my Stefan Kühn.

of the model, even if we restrict ourselves to a small number of degrees of freedom. The truncation of the bosonic fields does not severely affect the physics in the presence of a θ-term for the range of parameters we are interested in. In particular, even for very small system sizes that are accessible with current quantum hardware, we can observe the characteristic features of the phase structure. For large masses, or equivalently small values of R^2, the EFD and the ground state energy density clearly show the signatures of the first-order phase transition which eventually vanish as we go to small masses or correspondingly large R^2.

2.5 VQE with Parametric Cavities

In this section we discuss how the phase diagram of the one dimensional Higgs model with a topological term can be studied using current quantum simulators. As outlined in the introduction, we propose a VQE approach, which forgoes the need to implement the complicated interactions that appear in the Higgs model on the quantum simulator. Instead, the VQE protocol exploits a set of resource Hamiltonians that can be realized on a given platform and allows for the preparation of an output state that approximates the targeted ground state using the limited set of resource interactions available (see Appendix A). We target quantum simulations with parametric microwave cavities [50, 64], which have not been used for VQE so far, but are a promising candidate system as we explain below. In particular we first introduce the microwave platform and its features that makes it suitable

19

for our simulation in Section 2.5.1. We then present the specific resource Hamiltonian that can be engineered in the system, and the measurement scheme necessary to run the VQE in Section 2.5.3 and Section 2.5.4 respectively. We conclude by discussing the experimental imperfections and their role for the proposed simulation in Section 2.5.5. In the remainder of the chapter, Section 2.6 will provide a concrete protocol that allows for the study the effects previously discussed in Section 2.3.

2.5.1 Microwave-Photon Cavity

Here we detail the microwave-photonic hardware that we consider for our VQE of the U(1) Higgs Hamiltonian with a topological term. As shown schematically in Fig. 2.6, the quantum processor of our VQE scheme consists of a multimode coplanar waveguide resonator terminated by a SQUID at one end [50, 64]. The SQUID is coupled both to a microwave pump mode for classical control and to the total flux of the cavity. The SQUID - consisting of a superconducting loop with two Josephson junctions - provides a high degree of dissipationless, nonlinearity in the system. This basic element is the key to the success of superconducting computing architectures [65] and is used here to control microwave fields. In the VQE, each lattice site in the model corresponds to a mode on the experimental platform. In fact, in the multimode cavity the model's lattice is constructed in so-called "synthetic dimensions" in frequency space [66].

Using microwave photons as quantum degrees of freedom in a VQE has the advantage that a larger Hilbert space can be accessed compared to traditional, qubit-based VQE protocols. This property is a naturally good fit for the simulation of gauge or Higgs fields, which are defined on infinite dimensional Hilbert spaces. As a result, using bosonic degrees of freedom requires fewer experimental modes and avoids the translation of two-body terms into three- and four-body interactions, which usually occurs when when encoding multilevel gauge fields using qubits.

Additionally, as explained in Section 2.5.3 and Refs. [50, 64, 67], the SQUID circuit in the experimental setup is an important source for nonlinear interactions, and the pump mode provides a high degree of classical control on the available interactions. This means one can create highly-customizable gates: for example, by choosing to use a so-called symmetric SQUID [67], we can enhance the fourth-order nonlinearity while suppressing the third-order. In this chapter, we explain in detail only how to use the nonlinear operations to create interactions involving the product of four photonic operators (see Appendix E for details), which are necessary for the simulation of the Higgs model, but in principle these ideas can be extended much further. This flexibility is perfect for special purpose VQEs,
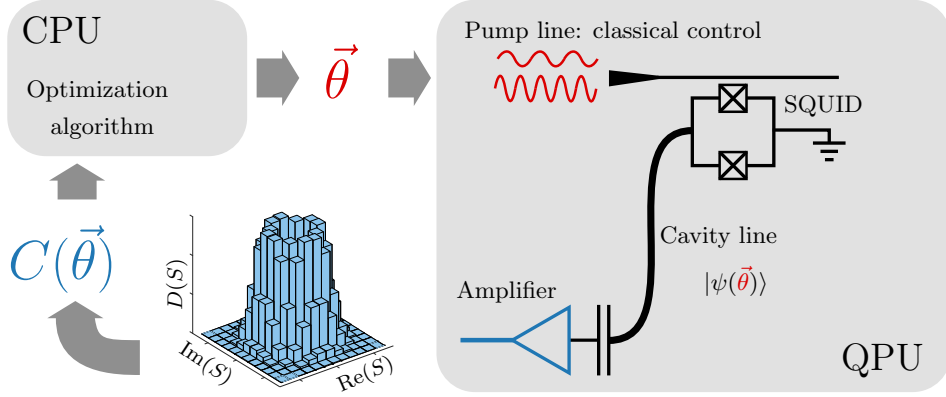
Figure 2.6: **Schematics of the VQE on the microwave-photon platform.** The quantum processor unit (QPU) consists of a microwave cavity terminated by a SQUID. The variational parameters $\vec{\theta}$ determine how the SQUID is pumped and consequently which interactions are generated between the cavity modes to generate the ansatz state $|\psi(\vec{\theta})\rangle$. A quantum-limited amplifier allows to perform heterodyne measurements on the cavity modes to obtain the cost function $C(\vec{\theta})$. In our case the cost function is the expectation value of the Hamiltonian for which we want to find the ground state, as defined in Eq. (2.26). $C(\vec{\theta})$ is used by the classical processor unit (CPU) to find the optimal variational parameters that minimizes it. This figure was made by Jinglei Zhang.

including the one considered in this chapter. In addition, it is natural for this platform to generate effective couplings that are complex (see Section 2.5.3 and Appendix E for details), which can be beneficial to VQEs of lattice gauge theories. Overall, our approach is complementary to existing VQE schemes in the sense that it has strikingly different features than qubit-based protocols, but also uses resource Hamiltonians that are different from other bosonic platforms, such as optical photons [68, 69] or ultracold atoms [70].

2.5.2 The HOBM Mapping

In order to simulate the Higgs Hamiltonian given in Eq. (2.14) with the microwave-photon cavity, its operators $\hat{Q}_n$ and $\hat{\phi}_n$ need to be mapped to the degrees of freedom of the chosen experimental platform. The mapping we used is called the Highly Occupied Boson Model (HOBM) [71] and is given by

$$\hat{Q}_n \to \hat{N}_n - N_0, \qquad \hat{\phi}_n \to \frac{1}{\sqrt{N_0}}\hat{a}_n, \tag{2.19}$$
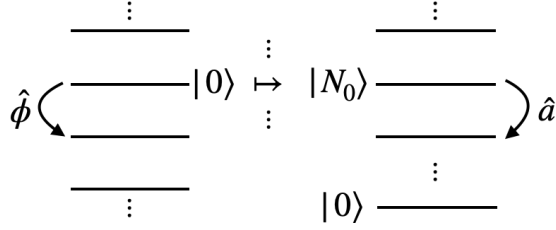
Figure 2.7: **Schematic of HOBM mapping.** The charge basis state (left) with charge Q $|Q\rangle$ is mapped to the Fock state (right) with $Q + N_0$ photons $|Q + N_0\rangle$ under the HOBM mapping. In the HOBM, $\hat{a}$ is proportional to the Higgs field operator $\hat{\phi}$ according to Eq. (2.19).

where $N_0 \in \mathbb{N}$ is a constant such that the zero charge state in the Higgs model maps to the Fock state with N_0 photons (see Fig. 2.7). $\hat{N}$ and $\hat{a}$ are the photonic number and lowering operators, respectively. With this mapping, the U(1) Higgs Hamiltonian becomes

$$
\begin{aligned}
\hat{H}_{\text{HOBM}} = & \sum_{n=1}^{N} \left(\frac{1}{2R^2} + \frac{N-n}{2\beta} \right) \hat{N}_n^2 - \frac{R^2}{2N_0} \sum_{n=1}^{N-1} \left(\hat{a}_n^\dagger \hat{a}_{n+1} + \text{H.C.} \right) + \sum_{n=2}^{N-1} \sum_{j=1}^{n-1} \frac{N-n}{\beta} \hat{N}_j \hat{N}_n \\
& + \sum_{n=1}^{N} \left(\frac{(N-n)(2\varepsilon_0 - N_0(N+n-1))}{2\beta} - \frac{N_0}{R^2} \right) \hat{N}_n \\
& - \beta(N-1) + \frac{\varepsilon_0^2}{2\beta}(N-1) + \frac{N_0^2 N}{2R^2} + \frac{N(N-1)N_0((2N-1)N_0 - 6\varepsilon_0)}{12\beta}.
\end{aligned}
\tag{2.20}
$$

When simulating the VQE on a classical computer, we must truncate the Hilbert space of every mode to include only the states with photon number $N_0 - k$ to $N_0 + k$ for some integer k. Let us consider the effects of using the untruncated and truncated mappings. In the following we will omit the lattice site index as these expressions hold for all sites. Using the untruncated HOBM model, all of the commutation relations remain the same (see Section 2.2.1 for the commutation relations of the original model), except for

$$
[\hat{\phi}, \hat{\phi}^\dagger] \to \frac{1}{N_0}.
\tag{2.21}
$$

The correct commutation relation should be $[\hat{\phi}, \hat{\phi}^\dagger] = 0$, which is recovered as $N_0 \to \infty$. Let $\hat{a}(k)$ and $\hat{N}(k)$ be the truncated operators (truncated to matrices of size $2k+1$). When

we consider the truncated HOBM model (as is the case for our classical simulation) an error is introduced and the following commutation relations can be derived

$$[\hat{Q}, \hat{\phi}^\dagger] \rightarrow \left[\hat{N}(k) - N_0, \frac{1}{\sqrt{N_0}} \hat{a}^\dagger(k) \right]$$
$$= \frac{1}{\sqrt{N_0}} \hat{a}^\dagger(k) + \frac{N_0 - k}{\sqrt{N_0}} \hat{a}^\dagger(k) |N_0 - k\rangle\langle N_0 - k|, \tag{2.22a}$$

$$[\hat{\phi}, \hat{\phi}^\dagger] \rightarrow \frac{1}{N_0} [\hat{a}(k), \hat{a}^\dagger(k)]$$
$$= \frac{1}{N_0} + \frac{N_0 - k}{N_0} |N_0 - k\rangle\langle N_0 - k| - \frac{N_0 + k + 1}{N_0} |N_0 + k\rangle\langle N_0 + k|. \tag{2.22b}$$

To recover the correct commutation relation in Eq. (2.22a), we set $k = N_0$, which gives

$$[\hat{Q}, \hat{\phi}^\dagger] \rightarrow \left[\hat{N}(k) - N_0, \frac{1}{\sqrt{N_0}} \hat{a}^\dagger(k) \right] = \frac{1}{\sqrt{N_0}} \hat{a}^\dagger(k), \tag{2.23a}$$

$$[\hat{\phi}, \hat{\phi}^\dagger] \rightarrow \frac{1}{N_0} \left[\hat{a}(k), \hat{a}^\dagger(k) \right] = \frac{1}{N_0} - \frac{2N_0 + 1}{N_0} |2N_0\rangle\langle 2N_0|. \tag{2.23b}$$

Eq. (2.23a) is the same commutation relation as in the full Hilbert space [Eq. (2.1)] and, given that $[\hat{\phi}, \hat{\phi}^\dagger] = 0$ in the full Hilbert space, the truncation error in Eq. (2.23b) goes to zero as $N_0 \rightarrow \infty$. In general, Eq. (2.23b) shows that the state with maximum photon number, $|2N_0\rangle$ is most affected by truncation errors.

2.5.3 Resource Hamiltonians

In this section we discuss the resource Hamiltonians that will be used in the VQE and how they can be generated by the microwave-photon platform's interaction Hamiltonian. By driving the pump at a frequency equal to the difference in the cavity mode frequencies of two modes c and d [50], we can create a $c - d$ beam splitter interaction (see Ref. [67] for details)

$$\hat{U}_{\text{BS}}^{(c,d)}(\theta, \vec{\Omega}, \lambda) = \exp\left(i\theta \left(e^{i\lambda} \hat{a}_c^\dagger \hat{a}_d + \text{H.C.} \right) + i \sum_{n=1}^{N} \Omega_n \hat{N}_n \right). \tag{2.24}$$

This type of interaction has been experimentally realized on the microwave-photon platform. The three types of variational parameters that appear in this Hamiltonian, θ, λ, and $\vec{\Omega}$, can be optimized by the classical algorithm and are set by classical control parameters.

In principle, one can apply the variational parameters on the considered platform by fixing the coupling strength and varying the time or vice-versa, though the former offers greater stability. θ is the product of the coupling strength (which is proportional to the intensity of the driving field) and the gate application time, and the relative phase λ is given by the phase of the pump signal. Ω_n is the product of the nth effective cavity mode frequency (which is set by our choice of reference frame) and the gate application time. Note that this interaction closely resembles the kinetic term in Eq. (2.20).

To create the second resource Hamiltonian, we exploit the ability of the SQUID to generate nonlinear interactions. For example, cubic nonlinear interactions have been experimentally demonstrated in Ref. [50]. The underlying principle can be extended by driving the SQUID at a frequency significantly lower than the effective cavity modes used. As described in Appendix E, this selects the following interaction while causing all other interactions to average to zero due to the rotating wave approximation:

$$\hat{U}_O(\theta, \vec{\Omega}) = \exp\left(i\theta\hat{H}_{\text{NN}} + i\sum_{n=1}^{N}\Omega_n\hat{N}_n\right), \tag{2.25a}$$

$$\hat{H}_{\text{NN}} = 6\sum_{n=1}^{N}\hat{N}_n\left(\hat{N}_n + 2N - 1\right) + 24\sum_{n=2}^{N}\sum_{j=1}^{n-1}\hat{N}_j\hat{N}_n. \tag{2.25b}$$

The explicit form of Eq. (2.25b) arises from the underlying SQUID Hamiltonian and is derived in Appendix E. The basic working principle to create such an interaction has been experimentally proven; based on experimental demonstrations so far, we expect that this interaction can be realized with coupling strength up to 10^7Hz [50, 72]. As before, θ is the product of the coupling strength (which is proportional to the effective interaction strength) and the gate application time, and Ω_n is the product of the nth effective cavity mode frequency and the gate application time. Importantly, this interaction contains terms like $\hat{N}_n$ and $\hat{N}_n^2$, both of which appear in the HOBM Higgs Hamiltonian Eq. (2.20). Since the target Hamiltonian $\hat{H}_{\text{HOBM}}$ lies in the Lie algebra spanned by the resource Hamiltonians give in Eqs. (2.24, 2.25a), the VQE will be able to reach the ground state of the theory [73, 74].

2.5.4 Measurements

In contrast to the optical domain, a natural measurement for microwave photons is linear amplification. The noise added during amplification is then a fundamental limit on the detection efficiency of microwave fields. Here we consider, in particular, a well-established

measurement available for microwave photons: the linear phase-insensitive amplifier, which simultaneously amplifies both quadratures of the input field [67, 75]. Quantum mechanics dictates that amplifying the field in a phase-insensitive manner adds at least one unit of vacuum noise to the signal. Once the signal is amplified, it is therefore natural to simultaneously measure two conjugate quadratures, since this does not affect the signal-to-noise ratio. The signal obtained is equivalent to a heterodyne measurement of the cavity modes. Additionally, higher-order coherence functions can also be calculated [76] (see Appendix E) to obtain statistics of nonlinear measurements that cannot be performed directly (for example, photon number measurements).

The quantum state emitted from the microwave cavity is amplified in the large gain limit (see Ref. [50] for details). Measuring the field quadratures at the two output ports corresponds to simultaneously measuring the self-adjoint part $\hat{X}_S = (\hat{S} + \hat{S}^\dagger)/2$ and the anti self-adjoint part $\hat{P}_S = (\hat{S} - \hat{S}^\dagger)/2$ of the signal operator

$$\hat{S} = \hat{a} + \hat{h}^\dagger.$$

Here $\hat{a}$ refers to the cavity output state $|\psi(\vec{\theta})\rangle$ to be measured (see Fig. 2.6) and $\hat{h}$ is the amplifier noise mode. Note that $\hat{S}$ is a normal operator, meaning $[\hat{S}, \hat{S}^\dagger] = [\hat{X}_S, \hat{P}_S] = 0$. Furthermore, the eigenvalues of $\hat{X}_S$ and $\hat{P}_S$ correspond to the real and imaginary parts of the eigenvalues of $\hat{S}$, respectively. Repeated preparation and detection of the output state of the cavity yields a measurement distribution $D(S)$ (shown in Fig. 2.6), from which any statistical moment of $\hat{S}$ and $\hat{S}^\dagger$ can be calculated [76].

During the VQE of the HOBM Higgs Hamiltonian $\hat{H}_{\text{HOBM}}$ in Eq. (2.20), the cost function $C(\vec{\theta}) = \langle\psi(\vec{\theta})|\hat{H}_{\text{HOBM}}|\psi(\vec{\theta})\rangle$ is calculated from the data comprising the measurement histogram $D(S)$. Therefore, we express the expectation value of the HOBM Higgs Hamiltonian in terms of the statistical moments of the measured signal operator $\hat{S}$,

$$\begin{aligned}
C(\vec{\theta}) &= \langle\psi(\vec{\theta})|\hat{H}_{\text{HOBM}}|\psi(\vec{\theta})\rangle \\
&= \sum_n c_n \langle\hat{S}_n^\dagger \hat{S}_n\rangle + \sum_n c_n' \langle(\hat{S}_n^\dagger)^2 \hat{S}_n^2\rangle \\
&+ \sum_{n,m} c_{n,m}'' \langle\hat{S}_n^\dagger \hat{S}_n \hat{S}_m^\dagger \hat{S}_m\rangle + \sum_n c_n''' \langle\hat{S}_n^\dagger \hat{S}_{n+1} + \hat{S}_n^\dagger \hat{S}_{n+1}\rangle.
\end{aligned} \tag{2.26}$$

The above mapping of the cost function can be obtained using

$$\langle (\hat{S}_n^\dagger)^j \hat{S}_n^j \rangle = \sum_{i=0}^{j} \binom{j}{i}^2 \langle (\hat{a}^\dagger)^j \hat{a}^j \rangle, \tag{2.27a}$$

$$\langle \hat{S}_n^\dagger \hat{S}_n \hat{S}_m^\dagger \hat{S}_m \rangle = \langle \hat{N}_n \hat{N}_m \rangle + \langle \hat{N}_n \rangle + \langle \hat{N}_m \rangle + 1, \tag{2.27b}$$

$$\langle \hat{S}_n^\dagger \hat{S}_{n+1} + \hat{S}_n \hat{S}_{n+1}^\dagger \rangle = \langle \hat{a}_n^\dagger \hat{a}_{n+1} + \hat{a}_n \hat{a}_{n+1}^\dagger \rangle, \tag{2.27c}$$

which assumes that the noise modes are in the vacuum state $|0\rangle$ (*i.e.* this is a quantum-limited measurement) and the noise is uncorrelated with the cavity output modes. Experimentally, one can extract the value of $C(\vec{\theta})$ from the measured data distributions $D(S)$ using the following expressions [77]

$$\langle (\hat{S}_n^\dagger)^j \hat{S}_n^j \rangle = \int_{S_n} |S_n|^{2j} D(S_n), \tag{2.28a}$$

$$\langle \hat{S}_n^\dagger \hat{S}_n \hat{S}_m^\dagger \hat{S}_m \rangle = \int_{S_n, S_m} |S_n|^2 |S_m|^2 D(S_n, S_m), \tag{2.28b}$$

$$\langle \hat{S}_n^\dagger \hat{S}_{n+1} + \hat{S}_n \hat{S}_{n+1}^\dagger \rangle$$
$$= \int_{S_n, S_{n+1}} (S_n^* S_{n+1} + S_n S_{n+1}^*) D(S_n, S_{n+1}). \tag{2.28c}$$

2.5.5 Measurement Budget and Experimental Errors

In a VQE, the cost function $C(\vec{\theta})$ must be computed many times by the quantum device over the course of the experiment. Each cost function evaluation involves the preparation of the initial state, applying a sequence of gates, and the measurement of the final VQE state (together, we refer to this as a shot). As statistical and amplification noise are present in the cost function evaluation, the number of measurements of the state M determines how accurately we know the cost function. In particular, the variance of the cost function is σ_H^2/M, where σ_H^2 is the intrinsic variance of the Hamiltonian. Therefore, a large number of measurements is required to minimize the noise of the cost function, which means the number of measurements that can be performed and the repetition rate are crucial quantities when designing an experiment.

Let us investigate the measurement budget for the microwave-photon platform in more detail, as it is very different from that of common VQE platforms. The time required to prepare the initial state can be very short, for example the fastest time to prepare the

Fock state $|2222\rangle$ is estimated to be on the order of 10^{-8}s [78]. All the gates in the circuit, including beam splitter [Eq. (2.24)] and the $\hat{H}_{NN}$ interactions [Eq. (2.25a)], must be applied in a time interval less shorter the cavity decay time, which ranges between 10^{-7}s and 10^{-4}s [79]. For a cavity with fixed coupling, the time required to measure the state is also limited by the cavity decay time, as we must allow the state to escape the cavity before measuring it. There is however the possibility to employ cavities with tunable coupling to the environment [79]; the cavity can be closed to have a long cavity lifetime time and opened for a fast measurement process. Assuming a tunable coupling, the readout time is negligible compared to the gate application time.

As a result, the time budget for a single shot is dominated by the coupling strength, which is on the order of 10^7Hz for the interactions considered in Section 2.5.3 [50, 72]. Assuming the VQE circuit consists of about ten gates and θ in Eqs. (2.24, 2.25a) is of order 1, as is the case of our VQE (see Section 2.6), the time for a single shot is therefore on the order of 10^{-6}s. One advantage of the microwave-photon platform over other potential VQE platforms is its ability to run continuously without the need for human intervention. As a result, ignoring the time required for classical computing in the VQE feedback loop, up to 10^{11} measurements can be collected in a single day.

This discussion has so far ignored the effects of experimental imperfections present on this platform. The sources of error on the microwave-photon platform are similar to other gate-based superconducting processors and as a result we can expect a similar performance. In particular, Ref. [75] achieved a two-qubit gate infidelity of 10^{-3} and Ref. [80] achieved a Fock state preparation infidelity of 10^{-1}. We can also expect similar improvements to the platform as large commercial entities continue to improve and develop gate-based quantum computers. In the three steps consisting of a shot - state preparation, gate application, and measurements - we therefore expect the latter to pose the biggest concern. To access the impact of experimental imperfections, a realistic simulation of the VQE was made, which takes the measurement errors fully into account. This is presented in the upcoming section.

2.6 Microwave VQE for U(1) Higgs Hamiltonian

So far, we have discussed the physics of the U(1) Higgs Hamiltonian with a topological term, and the microwave-photon platform we wish to implement the VQE on. This section will focus on the VQE protocol itself. In order to show that our protocol is experimentally viable, we perform a classical simulation of the VQE and use it to create a plot of the EFD, similar to Fig. 2.4(b) and 2.4(d). In Section 2.6.1 we explain the VQE protocol

intended to run on the microwave-photon platform. In Section 2.6.2 we discuss the results of our simulations and demonstrate that our proposed measurement budget is realistic for an experiment running on current quantum hardware.

2.6.1 VQE Procedure

In the following, we explain our VQE scheme for approximating the ground state of the U(1) Higgs Hamiltonian. As detailed below, we include in the simulation the noise added during amplification of the microwave signal, since it represents the main source of experimental errors for the considered setup (see Section 2.5 for more details) and leads to imperfect measurements of the cost functions.

In general, a VQE optimizes over the global space of all the variational parameters (see Appendix A for a general introduction to VQEs). However, in our case there are a large number of variational parameters, making the optimization challenging. Therefore, we designed an optimization protocol that recursively considers a subset of all the variation parameters. The VQE protocol is as follows. We define $\hat{B}_{c,d}(\vec{\theta}, \vec{\Omega}, \lambda)$ as the block operator for the c, d beam splitter

$$\hat{B}_{c,d}(\vec{\theta}, \vec{\Omega}, \lambda) = \hat{L}^{(4)} \hat{L}^{(3)} \hat{L}^{(2)} \hat{L}^{(1)}$$
$$\hat{L}^{(j)} = \hat{U}_O(\theta_{2j}, \vec{\Omega}) \hat{U}_{\mathrm{BS}}^{(c,d)}(\theta_{2j-1}, \vec{\Omega}, \lambda),$$

where $\vec{\theta}$, $\vec{\Omega}$, and λ are the variational parameters. We call each $\hat{L}^{(j)}$ a layer and as a result each block contains four layers and each layer consists of an application of Eqs. (2.24, 2.25a). In our VQE protocol, the first block acts on the initial state and the parameters in that block are optimized so that $\langle \hat{H}_{\mathrm{HOBM}} \rangle$ is minimized. This produces the optimal state for the first block, which is then used as the input state when the second block is applied. The variational parameters in this new block are optimized and the procedure continues until the parameters in the final block have been optimized. We refer to this final state as the VQE state, which we can use to approximate the ground state energy or the EFD. Note that a block consists of $N + 9$ variational parameters (eight θ's, N Ω's, and one λ). Additionally, notice that all operators used in the VQE protocol preserve photon number (in other words, they keep the VQE state in the zero charge subsector).

The experimental procedure is as follows. Our VQE is for $N_0 = 2$ and a lattice of size $N = 4$, so the experiment will use four modes. First, the initial state $|2222\rangle$ is prepared; this is the ground state of $\hat{H}_{\mathrm{HOBM}}$ in the limit when $R^2, \varepsilon_0 \to 0$. Then, the VQE protocol is applied as explained above. Following the measurement procedure described in Section

2.5.4, linear measurements are performed on the VQE state; M measurements are done and the outcomes are complied into a histogram. From the histogram, the expectation values of the powers of $\hat{S}^\dagger$ and $\hat{S}$ are calculated using Eqs. (2.28a, 2.28b, 2.28c). Assuming $N = 4$, the following expectation values need to be calculated: $\langle \hat{S}_i^\dagger \hat{S}_i \rangle$, $\langle (\hat{S}_i^\dagger \hat{S}_i)^2 \rangle$, $\langle \hat{S}_j^\dagger \hat{S}_{j+1} + \hat{S}_j \hat{S}_{j+1}^\dagger \rangle$, and $\langle \hat{S}_k^\dagger \hat{S}_k \hat{S}_m^\dagger \hat{S}_m \rangle$ for $i \in [1, 4]$, $j \in [1, 3]$, $k \in [1, m-1]$, and $m \in [2, 3]$. From these values, the expectation value of each term in Eq. (2.20) can be calculated using Eqs. (2.27a, 2.27b, 2.27c) and so $\langle \hat{H}_{\text{HOBM}} \rangle$ is known. This noisy $\langle \hat{H}_{\text{HOBM}} \rangle$ value is the cost function used by the classical optimizer to adjust the variational parameters in the VQE protocol.

To demonstrate that our VQE protocol is experimentally viable, we performed a classical simulation of this procedure. For this classical simulation we model the noise by a Gaussian distribution. Once the VQE state is prepared, $\langle \hat{H}_{\text{HOBM}} \rangle$ and $\text{Var}(\langle \hat{H}_{\text{HOBM}} \rangle)$ are computed. The cost function is then randomly sampled from a Gaussian distribution with mean $\langle \hat{H}_{\text{HOBM}} \rangle$ and variance $\text{Var}(\langle \hat{H}_{\text{HOBM}} \rangle)/M$. Our simulations have shown the probability distribution of the experimental procedure discussed above agrees well with a Gaussian for large M.

2.6.2 VQE Results

To demonstrate that the VQE can reproduce the phase transition of the theory, we classically simulated the VQE, as described in the previous section, for $R^2 = 0.3$ and $R^2 = 0.6$ and compared the results to the exact diagonalization EFD. Since the ground state for $R^2 = 0.3$ is relatively simple, only a single block $C_{1,4}$ is used in the VQE circuit. As explained in Appendix D, we expect the dominant term in the ground state for $R^2 = 0.3$ to transition from $|2222\rangle$ to $|1223\rangle$ at the phase transition point, thus the $\hat{B}_{1,4}$ block is well-suited for this plot. For $R^2 = 0.6$, the ground state is more complicated, especially where the dominant term in the ground state transitions from $|2222\rangle$ to $|1223\rangle$, and so multiple blocks are used. The choice of blocks for each point in the $R^2 = 0.6$ plot is motivated by our knowledge of the exact-diagonalization ground state, though it can also be obtained through trial and error. The blocks and number of measurements M used to create both plots are shown in Table 2.1. In general, the more difficult points (*e.g.* close to the transition point) are given a larger measurement budget.

All the data in our simulation was averaged over multiple VQE simulations, but the particularly difficult points also underwent classical post-processing. These difficult points occur whenever the ground state and first excited state energies are close to one another and the accuracy with which we know the cost function does not resolve the energy gap.

Experimental Conditions Used for VQE Plots				
R^2	ε_0	Blocks	M	Post Processing
0.3	0.5	1-4	$1.00 \cdot 10^5$	No
	1.0			
	1.4			
	1.8		$2.35 \cdot 10^6$	Yes
	2.0			No
0.6	0.5	1-2, 2-3	$1.00 \cdot 10^5$	
	0.85	1-4, 1-2, 2-3	$2.00 \cdot 10^6$	Yes
	1.0	1-4, 1-3, 2-4, 1-2		
	1.25	1-4, 1-3, 2-3, 2-4, 3-4	$1.00 \cdot 10^6$	No
	2.0	1-4, 2-3, 2-4		

Table 2.1: **Conditions used to generate the VQE data in Fig. 2.8.** The third column provides the sequence of blocks in the VQE circuit (for example, for $R^2 = 0.6$, $\varepsilon_0 = 0.5$, the 1-4 beam splitter was applied in the first block and the second block used the 2-4 beam splitter). The fourth column gives the number of measurements M used and the fifth column indicates whether post-processing was applied for that point in the figure.

As a result, the VQE may converge to the wrong state for these points. To combat this, we created a distribution of the final VQE state energies; if some of the energies are noticeably larger than the others, then the VQE targeted more the first excited state of $\hat{H}_{\mathrm{HOBM}}$ instead of the ground state in these trials. We then eliminated all data points corresponding to the fist excited state. The values of R^2 and ε_0 where we chose to use this post-processing technique are given in Table 2.1.

The VQE simulation results are shown in Fig. 2.8 for $N = 4$, $\beta = 1$, and $N_0 = 2$. For the purposes of the classical simulation we used a truncation of $k = 2$, though it is important to note that this is an error present only in our simulation of a VQE protocol. In Fig. 2.8(a) and 2.8(b), the EFD of the ground state is plotted against ε_0 for $R^2 = 0.3$ and $R^2 = 0.6$ respectively. The red dots represent the average EFD of ten VQE simulations, the error bars represent the standard deviation of those ten trials, and the blue curve is the EFD of the true ground state calculated via exact diagonalization. The $R^2 = 0.3$ plot features a sharp phase transition which is absent in the $R^2 = 0.6$ plot. These plots show good agreement between the VQE EFD and the exact diagonaliztion results. Therefore, our measurement budget was sufficient to overcome statistical errors and noise from the amplifier to accurately reproduce the ground state, particularly with a better accuracy

when ε_0 is not close to the transition point. A plot representing the VQE results in the limit where $M \to \infty$ is given in Appendix F, representing the best possible results this VQE protocol can produce.

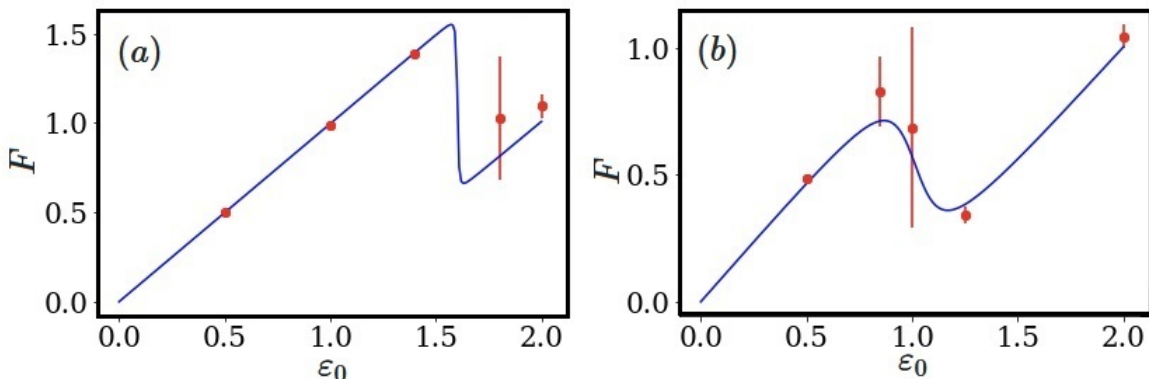Figure 2.8: **Higgs VQE simulation on microwave platform.** Electric field density F as a function of ε_0 for $\beta = 1.0$ and $R^3 = 0.3$ in *(a)* and $R^2 = 0.6$ in *(b)*. The blue line is the EFD of the exact diagonalization ground state and the red dots are the EFD of the VQE state. The dots represent the average EFD over ten simulations and the error bars represent the standard deviations. The beam splitter operations used in each block in the VQE are shown in Table 2.1.

Let us discuss the measurement budget of this protocol. The classical optimizer we employed to create Fig. 2.8 was a genetic algorithm and it needed $5 \cdot 10^4$ evaluations of the cost function to choose the optimal parameters for each block. The number of measurements used to build the histogram for each parameter set is given in Table 2.1. Using the data presented in Section 2.5.5 and assuming $M = 10^6$ measurements are used in each shot, a block can be optimized in about $4 \cdot 10^4$s. This means the $R^2 = 0.3$ VQE can be completed in about two days and the $R^2 = 0.6$ VQE can be completed in about ten days, assuming the VQE protocol is run only once per ε_0 value.

2.7 Conclusions

In this chapter we were able to demonstrate that the physical phenomena of the lattice Higgs model with a topological term, such as its first-order quantum phase transition, can be reproduced with a VQE running on currently-available quantum hardware. This is the first VQE of a lattice gauge theory with a topological term, which is important because

topological terms give rise to rich physics and they cannot be studied using conventional Markov Chain Monte Carlo lattice methods. Using MPS calculations, we studied the effects of a finite lattice size and truncated operators on the model. We designed a VQE protocol to be run on a microwave-photon platform, which is the first quantum simulation to do so and takes advantage of the specific interactions and number of measurements available on that platform. In our simulations of the VQE, we were able to capture the phase transition taking into account the measurement noise specific to the experimental system and showed that our VQE scheme is experimentally viable.

The next step is to perform the VQE detailed in this chapter on actual quantum hardware. As possible outlooks, one can use this work as a stepping stone towards studying a real time-evolution of the lattice Higgs model in 1+1 dimensions, perhaps to simulate interesting effects such as string breaking or to map out the phase diagram of the Higgs model with quenched systems. Given the features of the chosen experimental platform, this is in principle feasible in the near future. One could also expand on this work by designing and performing a VQE of the lattice Higgs model with a topological term in higher dimensions with the goal of reaching 3+1 dimensions. A VQE of a high-energy lattice gauge theory in three spatial dimensions is an important and ambitious milestone in the field of quantum simulation and a fundamental step towards answering some open questions about the universe.

Additionally, there are many exciting opportunities to use the unique features of the microwave-photon platform (as explained in Section 2.5.1) in future VQE experiments. For example, one is able to perform simultaneous, two-tone pumping on the platform [64], which would allow one to effectively combine two resource Hamiltonians. This technique was not used in our VQE protocol but it could greatly expand the types of interactions available for future VQEs. One could also perform a hybrid simulation that includes both qubits and bosons on the quantum hardware. This would be an excellent fit for a lattice gauge theory simulation that involves fermionic matter fields, for example. Given the highly tunable interactions available on this platform, it would also be suitable for VQEs of models outside of lattice gauge theories, including quantum chemistry and condensed matter physics.

Chapter 3

Measurement-Based Variational Quantum Eigensolvers

3.1   Introduction

Variational methods are crucial to investigate the physics of strongly correlated quantum systems. Powerful numerical tools like the density matrix renormalization group [1, 2, 3, 4] have been applied to several problems including real-time dynamics [81], condensed matter physics [82], lattice gauge theories [83, 84, 85, 86], and quantum chemistry [87, 88]. Nevertheless, the classes of states that can be studied with classical computers is severely limited [89]. Variational quantum eigensolvers (VQEs) overcome this problem using a closed feedback loop between a classical computer and a quantum processor [7, 8, 9]. The classical algorithm optimizes a cost function – typically the expectation value of some operator – which is efficiently provided by the quantum hardware. The VQE provides an approximation to the (low-lying) eigenvalues of this operator and the corresponding eigenstates. See Appendix A for a detailed introduction to VQEs. VQEs are advantageous for a variety of applications [9, 12, 15, 18, 90, 91, 92] and have been experimentally demonstrated in fields including chemistry [10, 11], particle physics [13, 14, 16, 17], and classical optimization [19].

   Existing VQE protocols are based on the circuit model, where gates are applied on an initial state [93]. These gates involve variational parameters whose optimization allows the resulting output state to approximate the desired target state. We propose a new approach to VQE protocols, based on the measurement-based model of quantum computation (MBQC) [24, 25, 26, 27, 28, 29]. In MBQC, an entangled state is prepared and the
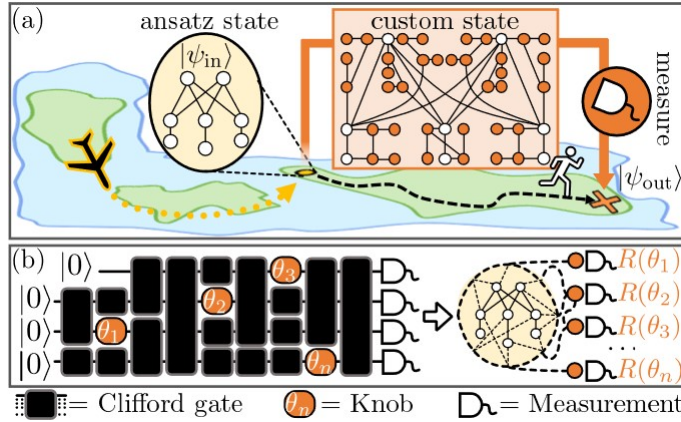
33

Figure 3.1: **MB-VQE schemes.** *(a)* Variation of a problem-specific ansatz state by 'edge decoration'. An ansatz graph state starts the MB-VQE in a suitable corner of Hilbert space (choice of green island). Next, a classical algorithm explores the neighbourhood (runner on black arrow). The variational optimization exploits a custom state that is obtained by decorating the edges of the ansatz state with auxiliary qubits (orange circles). Their measurement in rotated bases $R(\theta)$ with variational parameters θ transforms $|\psi_{\text{in}}\rangle$ into the output state $|\psi_{\text{out}}\rangle$. *(b)* Direct translation of a VQE circuit into a MB-VQE. *Left:* circuit consisting of Clifford gates (black) and single-qubit parametric gates ('knobs'). *Right:* corresponding MB-VQE, where the Clifford-part of the circuit has been performed beforehand. The custom state consists of output (white circles) and auxiliary (orange circles) qubits only; the latter are measured in rotated bases and are related to the 'knobs' in the circuit. This figure was made by Luca Dellantonio.

computation is realized by performing single-qubit measurements. While the circuit-based and measurement-based models both allow for universal quantum computation and have equivalent scaling of resources [27], they are intrinsically different. The former is limited by the number of available qubits and gates that can be performed, and MBQC by the size of the entangled state one can generate. For certain applications, the required coherence times [94, 95] and error thresholds [27, 94, 95, 96] are much less demanding for MBQC.

Here, we develop a new variational technique based on MBQC, that we call measurement-based VQE (MB-VQE). Our protocols determine the ground state of a target Hamiltonian, which is a prototypical task for VQEs with wide-ranging applications [7, 10, 12, 14, 15, 92, 97]. The underlying idea is to use a tailored entangled state that we call a 'custom state', which allows us to explore an appropriate corner of the system's Hilbert space [Fig. 3.1(a)]. This custom state includes auxiliary qubits which, once measured, modify the state of the

output qubits. The choices of the measurement bases, and the corresponding variational changes to the state, are controlled by a classical optimization algorithm. This approach differs conceptually and practically from standard VQE schemes since MB-VQE shifts the challenge from performing multi-qubit gates to creating an entangled initial state.

We present two different MB-VQE schemes and apply them to concrete problems. First, we introduce a novel method to construct variational state families, illustrated using the toric code model with local perturbations [98]. This model is equivalent to a two-dimensional, periodic Z_2 matter-free lattice gauge theory [30]. As Fig. 3.1(a) shows, we start from an ansatz state $|\psi_{\text{in}}\rangle$ in an appropriate corner of the Hilbert space. To explore this neighbourhood using a classical optimization algorithm, we introduce a custom state and apply measurement-based modifications of $|\psi_{\text{in}}\rangle$ that have no direct analogue in the circuit-model. The resulting variational family is not efficiently accessible with known classical methods and is more costly to access with circuit-based VQEs.

Second, we introduce a direct translation of circuit VQEs to MB-VQEs [Fig. 3.1(b)]. Here, the variational state family is the same for the circuit- and the measurement-based approach, but the implementation differs as the MB-VQE requires a resource state of reduced size and is manipulated by single-qubit measurements only. We exemplify this direct translation for the Schwinger model [31] and highlight the different hardware requirements and the scaling of resources. As explained below, a translation to MB-VQE is advantageous for circuits containing a large fraction of so-called Clifford gates (*e.g. CX* gates), as these are absorbed into the custom state.

While MB-VQE is platform agnostic, it opens the door for complex quantum computations in systems where long gate sequences or the realisation of entangling gates are challenging. In particular, MB-VQE offers new routes for experiments with photonic quantum systems, thus enlarging the toolbox of variational computations.

3.2   Fundamentals of MBQC

The main resource of MBQC are so-called graph states [99, 100], which are closely related to stabilizer states. An N-qubit stabilizer state $|\psi\rangle$ satisfies $\hat{S}|\psi\rangle = |\psi\rangle$ for all $\hat{S} \in V$, where V is a set of N independent, commuting N-fold tensor products of Pauli operators. Graphs as in Fig. 3.1 are stabilizer states of the operators $\hat{S}_n = \hat{X}_n \prod_k \hat{Z}_k$, where k refers to the vertices connected to vertex n by edges in the graph. Operationally, one can create a graph state by preparing $|+\rangle = \frac{1}{\sqrt{2}}(|0\rangle + |1\rangle)$ states for each vertex in the graph and then applying

CZ operations for each edge in the graph. However, this is not the only way to create a graph state. To obtain the desired final state encoded in the output qubits (white circles), single-qubit measurements are performed on auxiliary qubits (orange circles), either in the eigenbasis of the Pauli operators $\hat{X}$, $\hat{Y}$, $\hat{Z}$, or in the rotated basis $R(\theta) \equiv \{\frac{1}{\sqrt{2}}(|0\rangle \pm e^{i\theta}|1\rangle)\}$.

Depending on the measurement outcomes, the system is probabilistically projected into different resulting states. To render the computation deterministic, so-called byproduct operators and adaptive measurements are required [27]. For the former, we apply a byproduct operator $\hat{U}_{\Sigma} = \prod_i \hat{X}_i^{\alpha_i} \hat{Z}_i^{\beta_i}$ to the output state after all the measurements on the cluster have been performed. Note that α_i and β_i depend on the measurement outcomes and their exact form can be calculated following Theorem 1 in Ref. [27]. Additionally, the byproduct operators can be indirectly applied to the output state via classical post-processing. The latter involves adapting the measurement bases $R(\theta)$, potentially changing θ into $-\theta$ depending on previous measurement outcomes. Consequently, these adaptive measurements must be performed in a specific order.

An advantage of MBQC is the possibility to simultaneously perform all non-adaptive measurements at the beginning of the calculation [Fig. 3.1(b)]. This corresponds to the Clifford part of a circuit and includes single- and many-qubit gates. This is independent of the position of the gates in the circuit, and reduces the required overhead and coherence time. Remarkably, this can be either done directly on the graph state in the quantum hardware, or on a classical computer before the experiment. In the latter case, the Gottesmann-Knill theorem [101] allows for efficiently determining the custom state which is local-Clifford equivalent to the quantum state obtained after all non-adaptive measurements are performed [102]. Note that these local Clifford gates can be indirectly applied to the state by modifying the bases of the remaining adaptive measurements. This state can be directly prepared and used for the MBQC, which may have dramatically fewer auxiliary qubits compared to the initial graph state.

3.2.1 Examples of Measurement Patterns

In this section, we summarize the results of Ref. [27] which are relevant to the proposals put forward later in the text. In particular, we review how a universal set of gates can be realized in the MBQC framework.

In the following, we denote the measurement result on qubit n as $(-1)^{s_n}$, where $s_n \in \{0, 1\}$. A generic single-qubit unitary gate can be written as

$$\hat{U}(\theta_1, \theta_2, \theta_3) = \hat{U}_x(\theta_3)\hat{U}_z(\theta_2)\hat{U}_x(\theta_1), \tag{3.1}$$
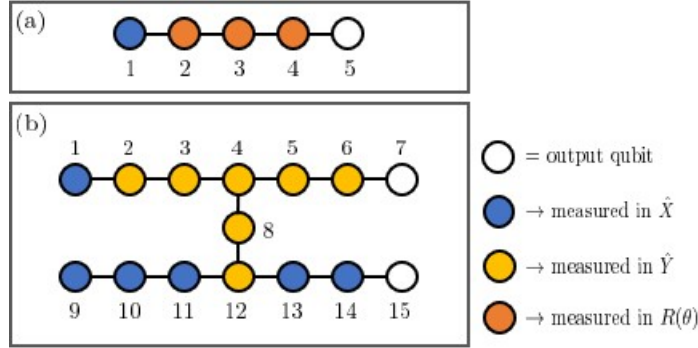
Figure 3.2: **Examples of gates in MBQC.** *(a)* Measurement pattern for a general single-qubit unitary operation. Qubit 1 is the input qubit. *(b)* Measurement pattern for the CX gate. Qubits 1 and 9 are the input qubits. This figure was made by Luca Dellantonio.

which corresponds to a rotation of an arbitrary angle around an arbitrary axis. The measurement pattern realizing this gate is shown in Fig. 3.2(a), where qubit 1 is the input qubit in a state $|\text{in}\rangle$, qubits 2, 3, and 4 are measured in the bases $R(-(-1)^{s_1}\theta_1)$, $R(-(-1)^{s_2}\theta_2)$, and $R(-(-1)^{s_1+s_3}\theta_3)$, respectively, and qubit 5 is the output qubit. Measuring the qubits in this order results in the final state of the output qubit $\hat{U}_\Sigma \hat{U}(\theta_1, \theta_2, \theta_3)|\text{in}\rangle$, where the byproduct operator $\hat{U}_\Sigma$ is

$$\hat{U}_\Sigma = \hat{X}^{s_2+s_4}\hat{Z}^{s_1+s_3}. \tag{3.2}$$

This is an example of adaptive measurements, since the measurement bases of qubits 2, 3, and 4 depend on previous results. By contrast, a CX gate acting on two qubits [see Fig. 3.2(b)] corresponds to a non-adaptive measurement pattern. In this case, the measurements can be performed in any order or simultaneously. The byproduct operators for the CX gate are

$$\hat{U}_\Sigma = \hat{X}_7^{s_2+s_3+s_5+s_6}\hat{Z}_7^{s_1+s_3+s_4+s_5+s_8+s_9+s_{11}+1}\hat{X}_{15}^{s_2+s_3+s_8+s_{10}+s_{12}+s_{14}}\hat{Z}_{15}^{s_9+s_{11}+s_{13}}, \tag{3.3}$$

and the output qubits are qubits 7 and 15.

While Fig. 3.2 explains how to implement individual gates in the MBQC formalism, one can implement a sequence of gates by concatenating the corresponding measurement patterns. In the remainder of this section, we explain how to merge measurement patterns. Assume that $\hat{A}$ and $\hat{B}$ are two gates, corresponding to two graph states with input, output and auxiliary qubits. In order to perform $\hat{B}\hat{A}$ in the MBQC framework, we combine the measurement patterns of $\hat{A}$ and $\hat{B}$ such that the input qubits of $\hat{B}$ are the same as the output qubits of $\hat{A}$. As a result, $\hat{B}\hat{A}$ has the same input qubits as $\hat{A}$ and the same output

qubits as $\hat{B}$. Let $\hat{U}_{\sigma A}$ and $\hat{U}_{\sigma B}$ be the respective byproduct operators and assume that $\hat{B}$ is a Clifford gate. Then, the overall byproduct operator is $\hat{U}_\Sigma = \hat{U}_{\sigma B}\hat{U}'_{\sigma A}$, where

$$\hat{U}_{\sigma B}\hat{B}\hat{U}_{\sigma A}\hat{A} = \hat{U}_{\sigma B}\hat{U}'_{\sigma A}\hat{B}\hat{A}, \tag{3.4a}$$

$$\hat{U}'_{\sigma A} = \hat{B}\hat{U}_{\sigma A}\hat{B}^\dagger. \tag{3.4b}$$

If instead $\hat{B}$ is a rotation gate [as in Eq. (3.1)], the overall byproduct operator is $\hat{U}_\Sigma = \hat{U}_{\sigma B}\hat{U}_{\sigma A}$, and

$$\hat{U}_{\sigma B}\hat{B}\hat{U}_{\sigma A}\hat{A} = \hat{U}_{\sigma B}\hat{U}_{\sigma A}\hat{B}'\hat{A}, \tag{3.5a}$$

$$\hat{B}' = \hat{U}_{\sigma A}\hat{B}\hat{U}_{\sigma A}. \tag{3.5b}$$

This modification of $\hat{B}$ affects the bases of the rotated measurements, which have to be fixed following the protocol in Ref. [27].

3.2.2 The Simulation Program

In order to simulate the preparation of a graph state and the measurements procedure, we wrote Python code. Classical simulations of quantum systems are generally inefficient and so this can only be done for small system sizes for demonstrative purposes. The parts of the code which work together to perform the MBQC computation are described here and shown in Fig. 3.3.

First, we need to prepare a graph state; the most straightforward way to do this is to specify the number of auxiliary qubits and the entanglement structure of the state. The program then prepares a number of qubits in the $|+\rangle$ and acts CZ gates on the specified qubits in order to produce the graph state. Note that the CZ gates, as well as all gates used by the program, are represented as sparse matrices to improve efficiency. However, it is also possible to create the initial graph state from a stabilizer state. Since every stabilizer state is equivalent to a graph state up to local Clifford gates (Hadamard and phase gates) [102], the program is also able to produce the initial graph state given a list of N complete, commuting stabilizers. The program follows the algorithm outlined in Theorem 1 in Ref. [102]; the algorithm is efficient and it outputs the equivalent graph state as well as the local Clifford gates.

Next, the Pauli (non-adaptive) measurements are performed on the initial graph state. This can be done efficiently (the size of the matrices scales linearly with the number of auxiliary qubits) following the procedure outlined in Ref. [101]. The program outputs a custom
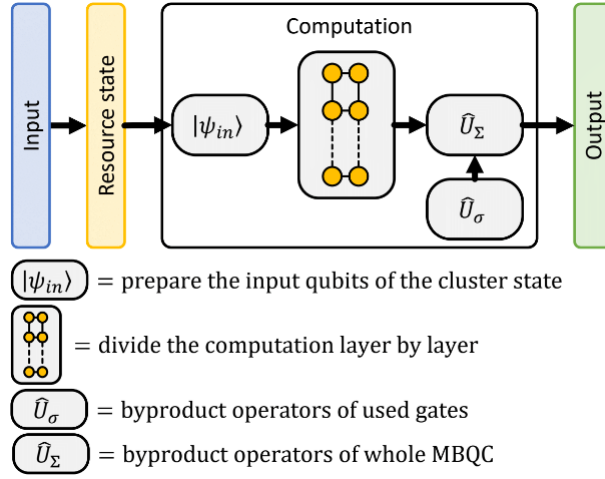
Figure 3.3: **Schematic for the MBQC simulation code.** First the graph state is prepared, then it is turned into a custom state by applying the Pauli measurements, and then the adaptive measurements are performed. Finally, byproduct operators act on the output state. This figure was made by Luca Dellantonio.

state; only the adaptive measurements need to be performed on this state. Depending on the number of Pauli measurements in the original measurement protocol, this procedure can greatly reduce the number of auxiliary qubits in the custom state, which means less computational power is needed to perform the remaining adaptive measurements.

The program is also able to take the byproduct operators $\hat{U}_\Sigma$ and adaptive measurements $R((-1)^\gamma \theta)$ into account. The byproduct operators and adaptive measurements for a single gate can be found in the literature [27] and some examples were given in Section 3.2.1, though the program is also able to calculate them following Theorem 1 in Ref. [27]. The program is also able to calculate the byproduct operators and adaptive measurements for a sequence of gates, following the procedure in Section 3.2.1. For each gate in the sequence, its byproduct operators are brought to the end of the sequence, getting transformed by the other gates as they move past them. Additionally, each time a byproduct operator moves past a gate consisting of adaptive measurements, those measurement bases are modified accordingly.

There are two protocols for performing the remaining adaptive measurements, given the custom state. In the more-direct approach, the entire custom state is created and then the adaptive measurements are performed on it sequentially. Each time a measurement is done, the remaining measurement bases are adjusted. Performing all the adaptive measurements

yields the state of the output qubits, not yet corrected by the byproduct operators. This part of the program is identical to what would happen in an experiment, but it has the disadvantage that the entire state, represented by a 2^N component vector, has to be stored and manipulated at once. Simulating adaptive measurements classically is inefficient and as a result this can only be done for small system sizes.

For the other protocol, we begin by generating only the input qubits (called layer 0) and the qubits adjacent to layer 0 in the graph (called layer 1). CZ gates are applied between the qubits in layers 0 and 1 where necessary and then the qubits in layer 0 are measured, which changes the states of the qubits in layer 1. Next, the qubits adjacent to the qubits in layer 1 in the graph (called layer 2) are introduced, the CZ gates are applied, and the qubits in layer 1 are measured. This sequential prepare-and-measure procedure is performed until only the output qubits remain. Even though this procedure is different in practice from what is done in an experiment, it produces an identical result [27]. This protocol is advantageous since only part of the custom state is generated at any given time. This is particularly beneficial if the custom state has a grid-like structure, such as the custom state in Fig. 3.2(b). Regardless of which protocol is used, the final step is to apply the byproduct operators to the output state.

3.3   State Variation by Edge Modification

Here, we demonstrate how MBQC tools – *i.e.* adding and measuring auxiliary qubits – can be used to design a MB-VQE that manipulates states in a completely different way than a circuit-based VQE. This MB-VQE is advantageous whenever a perturbation $\hat{H}_{\mathrm{p}}$ is added to a Hamiltonian $\hat{H}_0$ whose ground state, used as ansatz state $|\psi_{\mathrm{in}}\rangle$ below, is a stabilizer state or a graph state. Picking the ground state of $\hat{H}_0$ as ansatz is not necessary, but motivated by the fact that it corresponds to the desired outcome of the MB-VQE without perturbation.

3.3.1   Edge Modification Procedure

In this section, we explain how we decorate the edges of the ansatz state $|\psi_{\mathrm{in}}\rangle$ to obtain the custom state. The addition of the perturbation term $\hat{H}_{\mathrm{p}}$ can modify the entanglement structure in the ground state. Therefore, we need to decorate the edges of $|\psi_{\mathrm{in}}\rangle$ in such a way that, after the measurement of the auxiliary qubits, we both fine-tune the amount of entanglement between connected vertices and rotate the state of the output qubits. Though
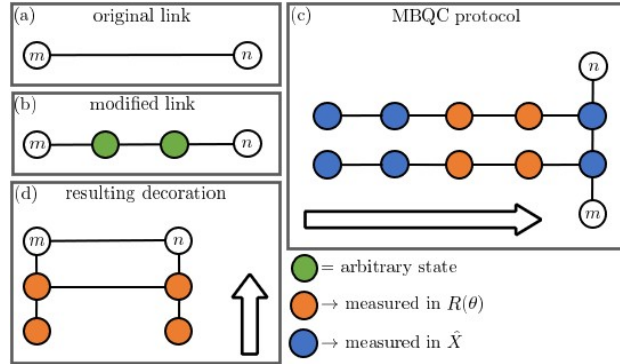
Figure 3.4: **Edge decoration scheme.** Schematic description of the edge decoration used for the perturbed toric code MB-VQE. The edge connecting a linked pair (m, n) of vertices in $|\psi_{\mathrm{in}}\rangle$ [shown in *(a)*] is decorated by adding two auxiliary qubits in an arbitrary state [shown in *(b)*]. The corresponding MBQC procedure prescribes the pattern in Section 3.2.1, resulting in the edge decoration protocol presented in *(c)*. By classically removing Clifford operations, we reduce the number of auxiliary qubits to be added to four, as shown in *(d)*. The arrows represent the temporal order in which the auxiliary qubits have to be measured. This figure was made by Luca Dellantonio.

the possibilities on how to add these auxiliary qubits are endless, we choose to follow the protocol given in Fig. 3.4. The idea is to decorate any edge connecting two output qubits with two auxiliary qubits in an arbitrary state [green circles in Fig. 3.4(b)], which are then measured in the $\hat{X}$ basis. If both these qubits are in the state $|+\rangle$, their measurement leaves the output qubits unaffected. However, if both auxiliary qubits are either in $|0\rangle$ or $|1\rangle$, their measurement eliminates all pre-existing entanglement between the original output qubits. For an arbitrary initial state of the two auxiliary qubits, the entanglement between the output qubits is generally reduced, and their wave vector rotated.

While it is possible to directly prepare the custom state with auxiliary qubits in arbitrary states, this does not create a graph state, and as such there are no known methods to obtain a deterministic outcome after the measurement of all auxiliary qubits. A formal MBQC protocol can be obtained by following the patterns in Section 3.2.1. Each of the auxiliary qubits to be used in the decoration is then substituted with five qubits, to be measured in a specific order [see Fig. 3.2(c)]. Since an arbitrary state can be prepared with only two measurements in rotated bases, out of the ten auxiliary qubits in Fig. 3.2(c), six can be eliminated [101]. The resulting state, presented in Fig. 3.2(d), only contains four auxiliary qubits per edge of the ansatz state.
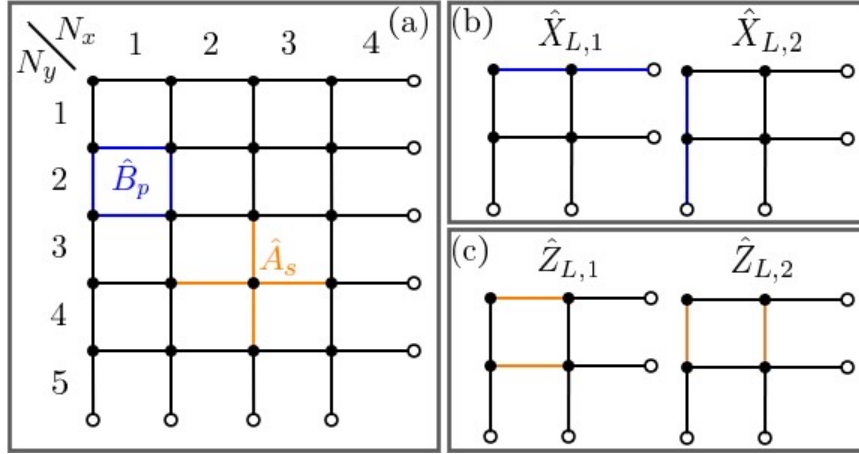
Figure 3.5: **Toric code notation.** *(a)* Toric code for $N_x = 4$ and $N_y = 5$. Qubits exist on the edges of the lattice, and two of the generators $\hat{A}_s$ and $\hat{B}_p$ are explicitly represented. Since the lattice lies on a torus, periodic boundary conditions are enforced, as shown by white circles. Schematic representations of the logical-X and logical-Z operators in the case $N_x = N_y = 2$ are given in *(b)* and *(c)*, respectively. In the whole figure, links colored in blue (orange) represent the action of the $\hat{X}$ ($\hat{Z}$) operator on the corresponding qubit. This figure was made by Luca Dellantonio.

Single-qubit rotations can also be implemented with additional auxiliary qubits connected to a chosen vertex, and multi-qubit operations by one or more auxiliary qubits connected to several vertices of the graph. While a completely deterministic manipulation can always be achieved by following MBQC rules [27], one can reduce the number of auxiliary qubits used in our scheme by allowing for a probabilistic manipulation.

After creating the custom state, auxiliary qubits are measured in a specific order to modify $|\psi_{\text{in}}\rangle$. The classical part of the VQE algorithm selects the rotated measurement bases $R(\theta)$ to minimize the energy $\langle \hat{H}_0 + \hat{H}_{\text{p}} \rangle$, calculated with respect to the output qubits. Generally, the more auxiliary qubits are added, the larger the variational class of states that the MB-VQE can reach. Just like the success of a circuit-based VQE is determined by the choice and number of gates used, a MB-VQE will be successful if the ground state can be efficiently reached by measuring the auxiliary qubits of the custom state.

3.3.2 Toric Code Hamiltonian VQE

We apply this MB-VQE approach to the toric code model, a quantum error-correcting code defined on a two-dimensional rectangular lattice with periodic boundary conditions [103]. This model is equivalent to a two-dimensional, periodic Z_2 matter-free lattice gauge theory [30]. On the lattice, the number of rows (columns) of independent vertices is N_x (N_y) and each edge represents a qubit. The toric code state is a stabilizer state of so-called star $\hat{A}_s$ and plaquette $\hat{B}_p$ operators. As shown in Fig. 3.5(a), for any vertex s in the lattice, $\hat{A}_s$ acts $\hat{Z}$ on the four incident edges, while $\hat{B}_p$ acts $\hat{X}$ on the four edges in the p-th plaquette. The toric code Hamiltonian is then $\hat{H}_0 = -\sum_s \hat{A}_s - \sum_p \hat{B}_p$. Since $\prod_s \hat{A}_s = \prod_p \hat{B}_p = 1$, the toric code has $2N_x N_y - 2$ independent stabilizers, and $\hat{H}_0$ has four degenerate ground states $|r,t\rangle_L$ ($r,t \in \{0,1\}$), called logical states below.

To explicitly write down these logical states, we add two extra stabilizers to the set of operators $\hat{A}_s$ and $\hat{B}_p$. There are two common choices for the pair of extra stabilizers to be added, which are called logical-X ($\hat{X}_{L,1}$ and $\hat{X}_{L,2}$) and logical-Z ($\hat{Z}_{L,1}$ and $\hat{Z}_{L,2}$), and are shown in Figs. 3.5(b) and 3.5(c), respectively. Explicitly, $\hat{Z}_{L,1}$ ($\hat{Z}_{L,2}$) acts $\hat{Z}$ on all horizontal (vertical) edges of an arbitrarily chosen column (row). Similarly, $\hat{X}_{L,1}$ ($\hat{X}_{L,2}$) acts $\hat{X}$ on all horizontal (vertical) edges of an arbitrarily chosen row (column). Both logical-X and logical-Z operators commute with all the other plaquette $\hat{B}_p$ and star $\hat{A}_s$ operators, but do not generally commute between themselves. The logical state $|r,t\rangle_L$ can then be defined as the unique ground state of $\hat{H}_0 - (-1)^r \hat{Z}_{L,1} - (-1)^t \hat{Z}_{L,2}$ ($r,t \in \{0,1\}$).

The perturbation added to the toric code Hamiltonian is

$$\hat{H}_{\mathrm{p}} = \sum_{n=1}^{2N_x N_y} \lambda_n \hat{Z}_n, \tag{3.6}$$

which corresonds to an inhomogeneous magnetic field. As ansatz state for the MB-VQE we choose $|\psi_{\mathrm{in}}\rangle = |0,0\rangle_L$, that approximates the ground state of $\hat{H}_0 + \hat{H}_{\mathrm{p}}$ for small positive values of λ_n (this can be proven with perturbation theory). The graph state representation of $|0,0\rangle_L$ can be calculated efficiently classically [102] and is shown in Fig. 3.6(a) for $N_x = N_y = 2$. However, if some of the weights λ_n are negative and/or the perturbation $\hat{H}_{\mathrm{p}}$ is changed to include other operators – like $\hat{X}$ – then $|0,0\rangle_L$ is not a good ansatz state anymore. Generally, the best ansatz state becomes a superposition $\sum_{r,t} c_{r,t} |r,t\rangle_L$, ($\sum_{r,t} |c_{r,t}|^2 = 1$; $r,t = 0,1$). To create this superposition, it is possible to use the generic $SU(4)$ rotation described in Ref. [104], with the logical-X and logical-Z operators as generators. Importantly, this $SU(4)$ rotation can be implemented in a MBQC fashion using
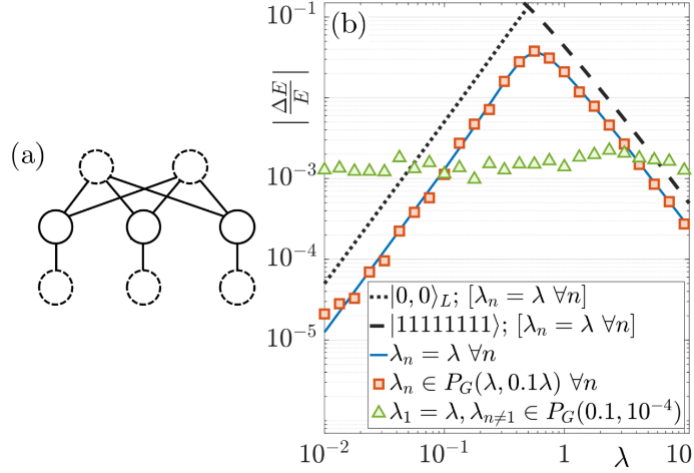
Figure 3.6: **Perturbed toric code.** *(a)* Graph state representation of the ansatz state $|0,0\rangle_L$. Additional Hadamard gates are applied to qubits with dashed lines. *(b)* Relative difference between the MB-VQE result and the true ground state energy vs the perturbation strength. We let λ_n in Eq. (3.6) be equal on all qubits (solid blue line), or sampled from a normal distribution P_G of average λ and variance 0.1λ (red squares). Green triangles describe a perturbation acting strongly on λ_1 and weakly on the other qubits. Dotted and dashed lines are computed with respect to $|0,0\rangle_L$ (ansatz state) and $|1\rangle^{\otimes 2N_x N_y}$ (ground state of $\hat{H}_p$) for $\lambda_n = \lambda \ \forall n$.

the tools described in Ref. [26]. The seven parameters describing this $SU(4)$ rotation can then be used as input parameters in the MB-VQE, such that the algorithm itself becomes capable of finding the best ansatz state within the degenerate subsector containing the four logical states.

As explained above, the custom state is obtained from the ansatz state by decorating edges with auxiliary qubits. For any pair (m,n) of qubits connected by an edge, we add four auxiliary qubits to ensure deterministic manipulation [see Fig. 3.4(d)]. Depending on the measurement bases $R(\theta)$, the entanglement between the qubits m and n is modified, and their state subjected to an additional rotation. For example, if all auxiliary qubits in the custom state are measured with $\theta = 0$, we obtain the original ansatz state. However, if all auxiliary qubits are measured with $\theta = \pi/2$, then all entanglement of the original ansatz state is eliminated.

Numerical results for the MB-VQE are shown in Fig. 3.6(b). The relative energy difference between the MB-VQE result and the true ground state (calculated via exact

diagonalization) is plotted against the perturbation strength. This is done with all λ_n in Eq. (3.6) equal to λ (solid blue line), with each λ_n drawn from a Gaussian distribution $P_G(\mu, \sigma^2)$ with mean $\mu = \lambda$ and variance $\sigma^2 = 0.1\lambda$ (orange squares), and with $\lambda_1 = \lambda$, λ_n randomly sampled from $P_G(\mu = 0.1, \sigma^2 = 10^{-4})$ for $n \neq 1$ (green triangles). A plot of the infidelity resembles Fig. 3.6(b), with maximum infidelities for the blue curve, red squares and green triangles being 6.2×10^{-2}, 6.5×10^{-2}, and 9.4×10^{-3}, respectively. Fig. 3.6(b) shows that the MB-VQE produces the ground state energy with high confidence when the perturbation strength is very small or very large. Notably, the MB-VQE outperforms the ansatz state (dotted black line) and the ground state of $\hat{H}_p$ in Eq. (3.6) (dashed black line) in all cases. If the perturbation only acts on one qubit, the chosen custom state allows the MB-VQE to find the exact ground state energy within machine precision. This is also the case if the perturbation acts on two disconnected qubits, provided we connect them and add auxiliary qubits as in Fig. 3.4(d). This suggests that the outcome of the MB-VQE can be significantly improved by adding few extra auxiliary qubits.

3.4 Translating VQEs into MB-VQEs

Instead of the approach described above, one can create a MB-VQE by translating the circuit of a VQE into its corresponding custom state and a sequence of measurements. Since a universal set of gates can be realized in a MBQC [27], any VQE can be translated into a MB-VQE. As we discuss below, this strategy is advantageous if the number of parametric adaptive measurements [*i.e.* 'knobs' in Fig. 3.1(b)] in the resulting MB-VQE scheme is small.

As an example, we determine the ground state energy of the so-called Schwinger model [31], a testbed used for benchmarking quantum simulations in high energy physics [13, 84, 105]. The Schwinger model describes quantum electrodynamics on a one-dimensional lattice; fermions are placed on the vertices of the lattice and the edges describe the electric fields. When open boundary conditions are used, one can eliminate the gauge fields at the expense of creating long-range interactions. By mapping the fermionic operators to Pauli spin operators, the Hamiltonian becomes [106, 107, 108]

$$
\begin{aligned}
\hat{H} = {} & \frac{J}{2} \sum_{n=1}^{S-2} \sum_{k=n+1}^{S-1} (S-k)\hat{Z}_n\hat{Z}_k - \frac{J}{2} \sum_{n=1}^{S-1} n\mathrm{mod}2 \sum_{k=1}^{n} \hat{Z}_k \\
& + w \sum_{n=1}^{S-1} \left(\hat{\sigma}_n^+ \hat{\sigma}_{n+1}^- + \mathrm{H.C.} \right) + \frac{\mu}{2} \sum_{n=1}^{S} (-1)^n \hat{Z}_n,
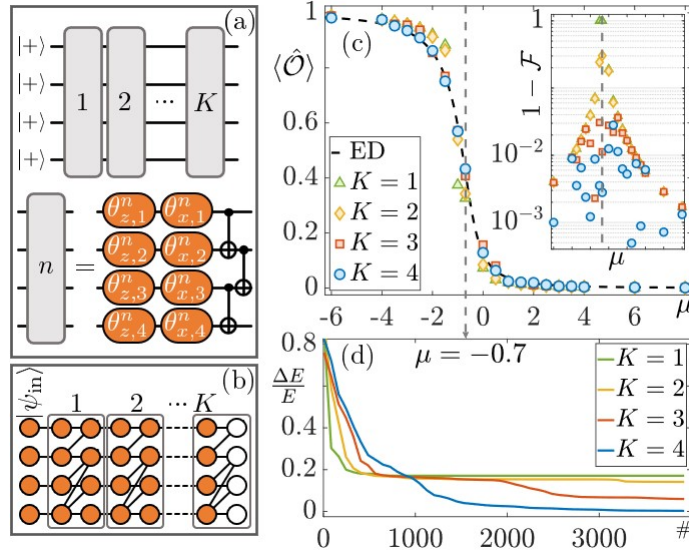\end{aligned}
\tag{3.7}
$$

45

Figure 3.7: **Schwinger model.** *(a)* Ansatz state and VQE circuit for $S = 4$ qubits and K layers. Each layer consists of CX gates and local rotations (orange) parametrized by angles $\theta_{\nu,i}^n$ (with rotation axis $\nu = x, z$; $i = 1, \ldots, 4$). *(b)* MB-VQE custom state for K layers. White circles are output qubits. Auxiliary qubits (orange) are measured in a rotated bases $R(\theta)$. *(c)* The order parameter $\langle \hat{\mathcal{O}} \rangle$ vs the fermion mass μ. The dashed line and dots represent exact diagonalization (ED) and (MB-)VQE results, respectively, with the number of layers K indicated in the legend. The inset shows the infidelity $1 - \mathcal{F}$. *(d)* Relative energy difference $\Delta E / E$ between (MB-)VQE results and ED for $\mu = -0.7$, versus the number of iterations in the optimization procedure. The variational parameters are initialized at zero, and $J = \omega = 1$ in Eq. (3.7). This plot was made by Abdulrahim Al Balushi.

where S is the number of fermions (it must be even), μ their mass, $w = \frac{1}{2a}$, and $J = \frac{g^2 a}{2}$. Here, a and g are the lattice spacing and the coupling strength, respectively, and $\hat{\sigma}_n^{\pm} = \frac{1}{2}(\hat{X}_n \pm i\hat{Y}_n)$.

For the VQE protocol, we assume the typical situation where parametric single-qubit gates and fixed entangling gates (CXs) are used [10, 109]. We consider a generic VQE circuit, in which a sequence of 'layers' is applied (see Ref. [7] and Appendix A), each containing local rotations and entangling gates. As shown in Fig. 3.7(a) for $S = 4$, we

choose the layer

$$\prod_{n=1}^{S/2-1} CX_{2n,2n+1} \prod_{n=1}^{S/2} CX_{2n-1,2n} \prod_{n=1}^{S} \hat{U}_{x,n}(\theta_{x,n})\hat{U}_{z,n}(\theta_{z,n}), \qquad (3.8)$$

where $\hat{U}_{\nu,n}(\theta_{\nu,n}) = \exp{(i\theta_{\nu,n}\hat{V}_n/2)}$ $[(\nu,\hat{V}) = (x,\hat{X})$ or $(\nu,\hat{V}) = (z,\hat{Z})]$. The circuit for the VQE is created by concatenating K layers, where K is big enough to sufficiently explore the relevant subsector of the considered Hilbert space. As described in Section 3.2.1, the MB-VQE custom state corresponding to a K-layer circuit is obtained by concatenating the measurement patterns of the gates in Eq. (3.8), and performing all non-adpative measurements classically, which effectively removes the Clifford parts of the circuit. The custom state is shown in Fig. 3.7(b). As ansatz state we use $|\psi_{\text{in}}\rangle = \bigotimes_{n=1}^{S}|+\rangle$.

The (MB-)VQE simulation results are shown in Fig. 3.7(c) for $S = 4$ and different values of K. We plot the order parameter $\langle\hat{\mathcal{O}}\rangle = \frac{1}{2S(S-1)}\sum_{i,j<i}\langle(1+(-1)^i\hat{Z}_i)(1+(-1)^j\hat{Z}_j)\rangle$ against the fermion mass μ and correctly observe a second-order phase transition around $\mu = -0.7$ [13, 71, 110]. Increasing K improves the ground state approximation, as demonstrated by the inset in Fig. 3.7(c) and by Fig. 3.7(d). The points near the phase transition require $K \gtrsim 3$ layers ($\gtrsim 28$ qubits), whereas $K = 1$ layer (12 qubits) suffices for the easiest points. Note that allowing different gates as resources in Eq. (3.8) generally leads to different convergence rates, as demonstrated by the results in Ref. [13].

Perfect platforms provided, both the VQE and the MB-VQE give the same result. However, the quantum hardware requirements are different for the two methods. The circuit-based VQE requires S qubits, $2KS$ single-qubit operations, and $K(S-1)$ entangling gates. For the corresponding MB-VQE, a custom state of $S(2K + 1)$ qubits and $2KS$ single-qubit operations (measurements) are required. Generally, translating a VQE into its corresponding MB-VQE is advantageous whenever the VQE circuit involves a large Clifford part and only a small number of adaptive measurements (*i.e.* knobs). In this case, MB-VQE avoids the requirement of performing long gate sequences, which is currently challenging due to error accumulation. This is especially interesting for platforms where entangling gates are hard to realize (*e.g.* photonic setups) or in systems with limited coherence times.

3.5 Conclusions

In this chapter, we combined the principles of measurement-based quantum computation and hybrid quantum-classical optimization. We presented two new types of variational

schemes. The first is useful when the ansatz state is a stabilizer state. In this case, it is classically efficient to determine the corresponding graph state [102], which can be decorated with additional control qubits and prepared directly. We applied this MB-VQE to the perturbed toric code. Additionally, we showed how to adapt any circuit-based VQE to become a MB-VQE, with the Schwinger model as example.

Experimental proof-of-concept demonstrations can be explored by considering the smallest instance of the planar code [103] with a perturbation on a single qubit as first step. In this scenario, the MB-VQE requires as few as eight entangled qubits instead of the 44 used above. This number can be further reduced by switching from a deterministic to a probabilistic protocol. Promising candidate systems include superconducting qubits, ions and Rydberg arrays, and photonic platforms. The latter recently demonstrated the capability to entangle several thousands of qubits [111, 112], and to create tailored graph states [113, 114, 115, 116]. When designing custom states for future experiments, it will be important to understand the effect of decoherence and it will be interesting to investigate whether MB-VQEs retain the high robustness of MBQC against errors [94, 95, 96].

Our scheme based on 'edge decorations' provides a new way of thinking about state variations in VQEs. In particular, the effect on the output qubits resulting from measuring only one or few entangled auxiliary qubits can be very challenging to describe with a simple circuit. The resulting state modifications do not necessarily correspond to unitary operations and can affect a large number of remaining qubits [26]. Accordingly, MB-VQEs can lead to schemes in which few auxiliary qubits suffice to reach the desired state, while many gates would be required in a circuit-based protocol. The effect of decorations can be studied further for tailored decorations, such as the possibility to add new edges to the entanglement structure. The framework presented here provides a starting point for designing VQEs whose properties are different and complementary to the standard approach that is based on varying a state by applying gates.

Conclusions

In this thesis, we used VQEs to simulate LGTs. We first considered a model with a topological term that is well-suited to be simulated on a photonic platform. Afterwards, we switched our focus on the VQE algorithm itself. We developed a novel measurement-based procedure and highlighted the differences and advantages if compared to existing techniques.

We presented the Hamiltonian of the U(1) Higgs lattice gauge theory in one spatial dimension with a topological term and used the Gauss law to eliminate the electric fields. We then described the phase structure of the model and the phase transition at $\varepsilon_0 = 1/2$ ($\theta = \pi$), which only occurs when R^2 is less than the critical value R_c^2. We investigated the ground state properties of the theory in various limits and analytically derived the corrections to the phase transition location due to finite size effects. We used MPS calculations to find the ground state of the theory for varying lattice sizes; by using the EFD and ground state energy density as order parameters we observed the phase transition. We found that the truncation of the operators has a lesser impact if compared to finite size effects. To efficiently study the ground state on current quantum hardware, a promising path was to use a VQE. Due to the bosonic nature of photons, we considered microwave-photonic systems for the quantum platform of the VQE. Moreover, recent experimental advances allow for a variety of non-linear interactions available for quantum simulations, and the experimental repetition rate is high. As a first step to perform a VQE, we cast the operators of the Higgs Hamiltonian into bosonic ladder operators. We then simulated a VQE with statistical and intrinsic quantum noise to study the phase transition for two values of R^2. In all cases we found good agreement between the order parameter given by the VQE and the exact diagonalization results, especially for ε_0 values far from the transition point. Importantly, we discussed the feasibility of our VQE on current hardware. For the Higgs VQE, there are two aspects which can be further investigated. First, the work in this thesis offers a clear path towards an experimental implementation. A realization of the protocols presented here would be exciting as the first VQE of a theory with a topological term and

the first VQE to run on a microwave-photon platform. Second, with the aim of eventually simulating and studying nature, it is necessary to extend the spatial dimensions of the U(1) Higgs model from one to three. This would bring us closer to solving the mystery of CP violation in the universe with quantum simulations. Additionally, the interactions and flexibility available on the microwave-photon platform makes it ideal for VQEs of other models in the future.

In the second part of the thesis, we introduced two possible MB-VQEs and compared them to circuit-based VQEs. We described a novel way to create a MB-VQE: starting with a graph state as an ansatz state, we decorated the edges with auxiliary qubits and measured them, thus modifying the entanglement between the qubits adjacent to the original edge. We explained how this procedure allows one to explore variational state families which cannot be efficiently accessed with known classical methods and are more costly to access with circuit-based VQEs. We noted that this technique is useful whenever the ground state of a perturbed Hamiltonian is sought and the ground state of the unperturbed Hamiltonian is a stabilizer state. As a result, we applied this technique to the toric code Hamiltonian with a local perturbation, which is equivalent to a two-dimensional, periodic Z_2 matter-free lattice gauge theory. For various perturbation types and strengths, we found good agreement between our VQE and the exact diagonalization results. Next, we explored a different method of creating a MB-VQE: by directly translating a circuit-based VQE to a graph state and a measurement scheme. Since MBQC allowed us to perform all the Clifford operations classically and efficiently on the initial graph state, we significantly reduced the number of auxiliary qubits needed for the ansatz graph state. We applied this technique to a VQE of the U(1) Schwinger lattice gauge theory in one spatial dimension and found the ground state with good fidelity for various choices of parameters. In particular, we compared the resources required for the circuit-based and MB-VQEs and noted how the MB-VQE has the advantage when there is a large number of Clifford gates in the VQE circuit. In general, any kind of MB-VQE is advantageous for platforms where it is difficult to perform long sequences of entangling gates (e.g. optical photons) or platforms with short coherence times. One can expand upon our MB-VQE work by investigating the effects of experimental noise on our protocols and further investigating different edge decoration strategies. For example, new edges can be added to the ansatz graph state and then decorated. An experimental implementation of MB-VQE, either using the decorated edges or the direct translation approach, would be an excellent continuation of the results presented in this thesis.

References

[1] D Perez-Garcia, F Verstraete, MM Wolf, and JI Cirac. Matrix product state representations. *Quant. Inf. Comput.*, 7:401, 2007.

[2] Jutho Haegeman, Tobias J. Osborne, and Frank Verstraete. Post-matrix product state methods: To tangent space and beyond. *Phys. Rev. B*, 88:075133, Aug 2013.

[3] Román Orús. Advances on tensor network theory: symmetries, fermions, entanglement, and holography. *Eur. Phys. J. B*, 87(11):280, 2014.

[4] G. Evenbly and G. Vidal. Tensor network renormalization. *Phys. Rev. Lett.*, 115:180405, Oct 2015.

[5] Tin Sulejmanpasic and Christof Gattringer. Abelian gauge theories on the lattice: θ-Terms and compact gauge theory with(out) monopoles. *Nucl. Phys. B*, 943:114616, 2019.

[6] Daniel Göschl, Christof Gattringer, and Tin Sulejmanpasic. The critical endpoint in the 2-d U(1) gauge-Higgs model at topological angle $\theta = \pi$. *PoS*, LATTICE2018:226, 2018.

[7] Jarrod R McClean, Jonathan Romero, Ryan Babbush, and Alán Aspuru-Guzik. The theory of variational hybrid quantum-classical algorithms. *New J. Phys.*, 18(2):023023, 2016.

[8] Edward Farhi, Jeffrey Goldstone, and Sam Gutmann. A quantum approximate optimization algorithm. *MIT-CTP/4610*, 2014.

[9] John Preskill. Quantum computing in the nisq era and beyond. *Quantum*, 2:79, 2018.

[10] Sam McArdle, Suguru Endo, Alán Aspuru-Guzik, Simon C. Benjamin, and Xiao Yuan. Quantum computational chemistry. *Rev. Mod. Phys.*, 92:015003, Mar 2020.

[11] P. J. J. O'Malley, R. Babbush, I. D. Kivlichan, J. Romero, J. R. McClean, R. Barends, J. Kelly, P. Roushan, A. Tranter, N. Ding, et al. Scalable quantum simulation of molecular energies. *Phys. Rev. X*, 6:031007, Jul 2016.

[12] E. F. Dumitrescu, A. J. McCaskey, G. Hagen, G. R. Jansen, T. D. Morris, T. Papenbrock, R. C. Pooser, D. J. Dean, and P. Lougovski. Cloud quantum computing of an atomic nucleus. *Phys. Rev. Lett.*, 120:210501, May 2018.

[13] Christian Kokail, Christine Maier, Rick van Bijnen, Tiff Brydges, Manoj K Joshi, Petar Jurcevic, Christine A Muschik, Pietro Silvi, Rainer Blatt, Christian F Roos, et al. Self-verifying variational quantum simulation of lattice models. *Nature*, 569(7756):355–360, 2019.

[14] Danny Paulson, Luca Dellantonio, Jan F Haase, Alessio Celi, Angus Kan, Andrew Jena, Christian Kokail, Rick van Bijnen, Karl Jansen, Peter Zoller, et al. Towards simulating 2d effects in lattice gauge theories on a quantum computer. *arXiv preprint arXiv:2008.09252*, 2020.

[15] Jan F Haase, Luca Dellantonio, Alessio Celi, Danny Paulson, Angus Kan, Karl Jansen, and Christine A Muschik. A resource efficient approach for quantum and classical simulations of gauge theories in particle physics. *arXiv preprint arXiv:2006.14160*, 2020.

[16] O. Shehab, K. Landsman, Y. Nam, D. Zhu, N. M. Linke, M. Keesan, R. C. Pooser, and C. Monroe. Toward convergence of effective-field-theory simulations on digital quantum computers. *Phys. Rev. A*, 100:062319, Dec 2019.

[17] Hsuan-Hao Lu, Natalie Klco, Joseph M. Lukens, Titus D. Morris, Aaina Bansal, Andreas Ekström, Gaute Hagen, Thomas Papenbrock, Andrew M. Weiner, Martin J. Savage, and Pavel Lougovski. Simulations of subatomic many-body physics on a quantum frequency processor. *Phys. Rev. A*, 100:012320, Jul 2019.

[18] Mari Carmen Bañuls, Rainer Blatt, Jacopo Catani, Alessio Celi, Juan Ignacio Cirac, Marcello Dalmonte, Leonardo Fallani, Karl Jansen, Maciej Lewenstein, Simone Montangero, et al. Simulating lattice gauge theories within quantum technologies. *Eur. Phys. J. D*, 74(8):1–42, 2020.

[19] Ajinkya Borle, Vincent E Elfving, and Samuel J Lomonaco. Quantum approximate optimization for hard problems in linear algebra. *arXiv preprint arXiv:2006.15438*, 2020.

[20] Carlos Bravo-Prieto, Ryan LaRose, Marco Cerezo, Yigit Subasi, Lukasz Cincio, and Patrick Coles. Variational quantum linear solver: A hybrid algorithm for linear systems. *Bulletin of the American Physical Society*, 65, 2020.

[21] Daniel González-Cuadra, Erez Zohar, and J. Ignacio Cirac. Quantum simulation of the abelian-higgs lattice gauge theory with ultracold atoms. *New J. Phys.*, 19(6):063038, 2017.

[22] Andrew G. Cohen, D.B. Kaplan, and A.E. Nelson. Progress in electroweak baryogenesis. *Ann. Rev. Nucl. Part. Sci.*, 43:27–70, 1993.

[23] M. Anosova, C. Gattringer, D. Göschl, T. Sulejmanpasic, and P. Törek. Topological terms in abelian lattice field theories. *PoS*, LATTICE2019:082, 2019.

[24] Robert Raussendorf and Hans J. Briegel. A one-way quantum computer. *Phys. Rev. Lett.*, 86:5188–5191, May 2001.

[25] Hans J Briegel, David E Browne, Wolfgang Dür, Robert Raussendorf, and Maarten Van den Nest. Measurement-based quantum computation. *Nature Phys.*, 5(1):19–26, 2009.

[26] Dan E Browne and Hans J Briegel. One-way quantum computation—a tutorial introduction, 2006. *arXiv preprint quant-ph/0603226*, 2006.

[27] Robert Raussendorf, Daniel E. Browne, and Hans J. Briegel. Measurement-based quantum computation on cluster states. *Phys. Rev. A*, 68:022312, Aug 2003.

[28] Philip Walther, Kevin J Resch, Terry Rudolph, Emmanuel Schenck, Harald Weinfurter, Vlatko Vedral, Markus Aspelmeyer, and Anton Zeilinger. Experimental one-way quantum computing. *Nature*, 434(7030):169–176, 2005.

[29] Mikkel V Larsen, Xueshi Guo, Casper R Breum, Jonas S Neergaard-Nielsen, and Ulrik L Andersen. Deterministic multi-mode gates on a scalable photonic quantum computing platform. *arXiv preprint arXiv:2010.14422*, 2020.

[30] L. Tagliacozzo and G. Vidal. Entanglement renormalization and gauge symmetry. *Phys. Rev. B*, 83:115127, Mar 2011.

[31] Julian Schwinger. The theory of quantized fields. i. *Phys. Rev.*, 82(6):914, 1951.

[32] F. Verstraete, V. Murg, and J.I. Cirac. Matrix product states, projected entangled pair states, and variational renormalization group methods for quantum spin systems. *Adv. Phys.*, 57(2):143–224, 2008.

[33] Ulrich Schollwöck. The density-matrix renormalization group in the age of matrix product states. *Ann. Phys.*, 326(1):96, 2011.

[34] Román Orús. A practical introduction to tensor networks: Matrix product states and projected entangled pair states. *Ann. Phys.*, 349:117 – 158, 2014.

[35] Sinya Aoki, Yasumichi Aoki, D Bečirević, Claude Bernard, Tom Blum, Gilberto Colangelo, Michele Della Morte, P Dimopoulos, Stephan Dürr, Hidenori Fukaya, et al. Review of lattice results concerning low-energy particle physics. *Eur. Phys. J. C*, 77(2):1–228, 2017.

[36] S Aoki, Y Aoki, D Bečirević, T Blum, Gilberto Colangelo, S Collins, M Della Morte, P Dimopoulos, S Dürr, H Fukaya, et al. Flag review 2019. *Eur. Phys. J. C*, 80(2):1–268, 2020.

[37] Matthias Troyer and Uwe-Jens Wiese. Computational complexity and fundamental limitations to fermionic quantum monte carlo simulations. *Phys. Rev. Lett.*, 94(17):170201, 2005.

[38] Christof Gattringer and Kurt Langfeld. Approaches to the sign problem in lattice field theory. *Int. J. Mod. Phys. A*, 31(22):1643007, 2016.

[39] Shahida Dar. The neutron edm in the sm: A review. *arXiv preprint hep-ph/0008248*, 2000.

[40] Maxim Pospelov and Adam Ritz. Electric dipole moments as probes of new physics. *Ann. Phys.*, 318(1):119–169, 2005.

[41] Boye Buyens, Simone Montangero, Jutho Haegeman, Frank Verstraete, and Karel Van Acoleyen. Finite-representation approximation of lattice gauge theories at the continuum limit with tensor networks. *Phys. Rev. D*, 95:094509, May 2017.

[42] Lena Funcke, Karl Jansen, and Stefan Kühn. Topological vacuum structure of the schwinger model with matrix product states. *Phys. Rev. D*, 101:054507, Mar 2020.

[43] Timo Felser, Pietro Silvi, Mario Collura, and Simone Montangero. Two-dimensional quantum-link lattice quantum electrodynamics at finite density. *arXiv preprint arXiv:1911.09693*, 2019.

[44] Christian Kokail, Christine Maier, Rick van Bijnen, Tiff Brydges, Manoj K. Joshi, Petar Jurcevic, Christine A. Muschik, Pietro Silvi, Rainer Blatt, Christian F. Roos, and Peter Zoller. Self-verifying variational quantum simulation of the lattice schwinger model. *arXiv:1810.03421*, 2018.

[45] Eduardo Fradkin and Stephen H. Shenker. Phase diagrams of lattice gauge theories with higgs fields. *Phys. Rev. D*, 19(12):3682, jun 1979.

[46] D. R. T. Jones, John Kogut, and D. K. Sinclair. Electrodynamics of the planar model: Its phase diagram, continuum limit, and mass spectrum. *Phys. Rev. D*, 19(6):1882–1905, mar 1979.

[47] Daniel Göschl. Dual simulation of the massless lattice schwinger model with topological term and non-zero chemical potential. In *EPJ Web of Conferences*, volume 175, page 07002. EDP Sciences, 2018.

[48] Ikuo Ichinose and Tetsuo Matsui. Lattice gauge theory for condensed matter physics: ferromagnetic superconductivity as its example. *Mod. Phys. Lett. B*, 28(22):1430012, aug 2014.

[49] Zohar Komargodski, Adar Sharon, Ryan Thorngren, and Xinan Zhou. Comments on abelian higgs models and persistent order. *SciPost Phys.*, 6:3, 2019.

[50] C. W. Sandbo Chang, Carlos Sabín, P. Forn-Díaz, Fernando Quijandría, A. M. Vadiraj, I. Nsanzineza, G. Johansson, and C. M. Wilson. Observation of Three-Photon Spontaneous Parametric Down-Conversion in a Superconducting Parametric Cavity. *Phys. Rev. X*, 10(1):011011, January 2020.

[51] S. R. Coleman. The uses of instantons. *Subnucl. Ser.*, 15:805, 1979.

[52] C. J. Hamer, Zheng Weihong, and J. Oitmaa. Series expansions for the massive schwinger model in hamiltonian lattice theory. *Phys. Rev. D*, 56:55–67, Jul 1997.

[53] M. C. Bañuls, K. Cichy, K. Jansen, and J. I. Cirac. The mass spectrum of the schwinger model with matrix product states. *J. High Energy Phys.*, 2013(11):158, 2013.

[54] Esteban A. Martinez, Christine A. Muschik, Philipp Schindler, Daniel Nigg, Alexander Erhard, Markus Heyl, Philipp Hauke, Marcello Dalmonte, Thomas Monz, Peter Zoller, and Rainer Blatt. Real-time dynamics of lattice gauge theories with a few-qubit quantum computer. *Nature*, 534(7608):516–519, June 2016.

[55] Christine Muschik, Markus Heyl, Esteban Martinez, Thomas Monz, Philipp Schindler, Berit Vogell, Marcello Dalmonte, Philipp Hauke, Rainer Blatt, and Peter Zoller. U(1) Wilson lattice gauge theories in digital quantum simulators. *New J. Phys.*, 19(10):103020, 2017.

[56] Jochen Heitger. *Numerical Simulations of Gauge-Higgs Models on the Lattice.* PhD thesis, Westfälische Wilhelms-Universität Münster, 1997.

[57] Christof Gattringer, Daniel Göschl, and Tin Sulejmanpašić. Dual simulation of the 2d u(1) gauge higgs model at topological angle $\theta = \pi$: Critical endpoint behavior. *Nucl. Phys. B*, 935:344–364, oct 2018.

[58] Tin Sulejmanpasic, Daniel Daniel Göschl, and Christof Gattringer. First-principle simulations of 1+ 1d quantum field theories at $\theta = \pi$ and spin-chains. *arXiv preprint arXiv:2007.06323*, 2020.

[59] Cliff Burgess and Guy Moore. *The standard model: A primer.* Cambridge University Press, 2007.

[60] F. Verstraete, D. Porras, and J. I. Cirac. Density matrix renormalization group and periodic boundary conditions: A quantum information perspective. *Phys. Rev. Lett.*, 93:227205, Nov 2004.

[61] Mari Carmen Bañuls, Krzysztof Cichy, J. Ignacio Cirac, Karl Jansen, and Stefan Kühn. Density induced phase transitions in the schwinger model: A study with matrix product states. *Phys. Rev. Lett.*, 118:071601, Feb 2017.

[62] Pablo Sala, Tao Shi, Stefan Kühn, Mari Carmen Bañuls, Eugene Demler, and Juan Ignacio Cirac. Variational study of u(1) and su(2) lattice gauge theories with gaussian states in 1+1 dimensions. *Phys. Rev. D*, 98:034505, Aug 2018.

[63] Mari Carmen Bañuls and Krzysztof Cichy. Review on novel methods for lattice gauge theories. *Rep. Prog. Phys.*, 83(2):024401, jan 2020.

[64] C. W. Sandbo Chang, M. Simoen, José Aumentado, Carlos Sabín, P. Forn-Díaz, A. M. Vadiraj, Fernando Quijandría, G. Johansson, I. Fuentes, and C. M. Wilson.

Generating Multimode Entangled Microwaves with a Superconducting Parametric Cavity. *Phys. Rev. App.*, 10(4):044019, October 2018.

[65] Göran Wendin. Quantum information processing with superconducting circuits: a review. *Rep. Prog. Phys.*, 80(10):106001, 2017.

[66] Luqi Yuan, Qian Lin, Meng Xiao, and Shanhui Fan. Synthetic dimension in photonics. *Optica*, 5(11):1396–1405, 2018.

[67] C. W. S. Chang. *Two-photon and Three-photon Parametric Interactions in Superconducting Microwave Circuits*. PhD thesis, University of Waterloo, 2019.

[68] Emanuel Knill, Raymond Laflamme, and Gerald J Milburn. A scheme for efficient quantum computation with linear optics. *Nature*, 409(6816):46–52, 2001.

[69] Pieter Kok, William J Munro, Kae Nemoto, Timothy C Ralph, Jonathan P Dowling, and Gerard J Milburn. Linear optical quantum computing with photonic qubits. *Rev. Mod. Phys.*, 79(1):135, 2007.

[70] Immanuel Bloch, Jean Dalibard, and Sylvain Nascimbene. Quantum simulations with ultracold quantum gases. *Nat. Phys.*, 8(4):267–276, 2012.

[71] Dayou Yang, Gouri Shankar Giri, Michael Johanning, Christof Wunderlich, Peter Zoller, and Philipp Hauke. Analog quantum simulation of $(1+1)$-dimensional lattice qed with trapped ions. *Phys. Rev. A*, 94:052321, Nov 2016.

[72] A Grimm, NE Frattini, S Puri, SO Mundhada, S Touzard, M Mirrahimi, SM Girvin, S Shankar, and MH Devoret. Stabilization and operation of a kerr-cat qubit. *Nature*, 584(7820):205–209, 2020.

[73] W.-L. Chow. über systeme von linearen partiellen differential-gleichungen erster ordnung. *Math. Ann.*, 117:98, 1940.

[74] Garng M Huang, Tzyh J Tarn, and John W Clark. On the controllability of quantum-mechanical systems. *J. Math. Phys.*, 24(11):2608–2618, 1983.

[75] Jay M Gambetta, Jerry M Chow, and Matthias Steffen. Building logical qubits in a superconducting quantum computing system. *npj Quantum Inf.*, 3(1):1–7, 2017.

[76] Marcus P. da Silva, Deniz Bozyigit, Andreas Wallraff, and Alexandre Blais. Schemes for the observation of photon correlation functions in circuit QED with linear detectors. *Phys. Rev. A*, 82(4):043804, October 2010.

[77] Christopher Eichler, Deniz Bozyigit, and Andreas Wallraff. Characterizing quantum microwave radiation and its entanglement with superconducting qubits using linear detectors. *Phys. Rev. A*, 86(3):032106, 2012.

[78] Zijun Chen, Julian Kelly, Chris Quintana, R. Barends, B. Campbell, Yu Chen, B. Chiaro, A. Dunsworth, A. G. Fowler, E. Lucero, E. Jeffrey, A. Megrant, J. Mutus, M. Neeley, C. Neill, P. J. J. O'Malley, P. Roushan, D. Sank, A. Vainsencher, J. Wenner, T. C. White, A. N. Korotkov, and John M. Martinis. Measuring and suppressing quantum state leakage in a superconducting qubit. *Phys. Rev. Lett.*, 116:020501, Jan 2016.

[79] Christopher S. Wang, Jacob C. Curtis, Brian J. Lester, Yaxing Zhang, Yvonne Y. Gao, Jessica Freeze, Victor S. Batista, Patrick H. Vaccaro, Isaac L. Chuang, Luigi Frunzio, Liang Jiang, S. M. Girvin, and Robert J. Schoelkopf. Efficient multiphoton sampling of molecular vibronic spectra on a superconducting bosonic processor. *Phys. Rev. X*, 10:021060, Jun 2020.

[80] Marios Kounalakis, Yaroslav M Blanter, and Gary A Steele. Synthesizing multi-phonon quantum superposition states using flux-mediated three-body interactions with superconducting qubits. *npj Quantum Inf.*, 5(1):1–7, 2019.

[81] Fabian Güttge, Frithjof B. Anders, Ulrich Schollwöck, Eitan Eidelstein, and Avraham Schiller. Hybrid nrg-dmrg approach to real-time dynamics of quantum impurity systems. *Phys. Rev. B*, 87:115115, Mar 2013.

[82] Yin-Chen He, Michael P. Zaletel, Masaki Oshikawa, and Frank Pollmann. Signatures of dirac cones in a dmrg study of the kagome heisenberg model. *Phys. Rev. X*, 7:031020, Jul 2017.

[83] Mari Carmen Banuls, Krzysztof Cichy, J. Ignacio Cirac, Karl Jansen, and Hana Saito. Matrix Product States for Lattice Field Theories. *PoS*, LATTICE 2013:332, 2014.

[84] Mari Carmen Bañuls and Krzysztof Cichy. Review on novel methods for lattice gauge theories. *Rep. Prog. Phys.*, 83(2):024401, 2020.

[85] Marcello Dalmonte and Simone Montangero. Lattice gauge theory simulations in the quantum information era. *Contemp. Phys.*, 57(3):388–412, 2016.

[86] Julian Bender, Patrick Emonts, Erez Zohar, and J Ignacio Cirac. Real-time dynamics in 2+ 1d compact qed using complex periodic gaussian states. *arXiv preprint arXiv:2006.10038*, 2020.

[87] Garnet Kin-Lic Chan, Jonathan J Dorando, Debashree Ghosh, Johannes Hachmann, Eric Neuscamman, Haitao Wang, and Takeshi Yanai. An introduction to the density matrix renormalization group ansatz in quantum chemistry. In S. Wilson, P. J. Grout, J. Maru-ani, G. Delgado-Barrio, and P. Piecuch, editors, *Frontiers in quantum systems in chemistry and physics*, volume 18 of *Progress in Theoretical Chemistry and Physics*, pages 49–65. Springer, 2008.

[88] C. Krumnow, L. Veis, Ö. Legeza, and J. Eisert. Fermionic orbital optimization in tensor network states. *Phys. Rev. Lett.*, 117:210402, Nov 2016.

[89] G. Ortiz, J. E. Gubernatis, E. Knill, and R. Laflamme. Quantum algorithms for fermionic simulations. *Phys. Rev. A*, 64:022319, Jul 2001.

[90] Omar Shehab, Isaac H Kim, Nhung H Nguyen, Kevin Landsman, Cinthia H Alderete, Daiwei Zhu, C Monroe, and Norbert M Linke. Noise reduction using past causal cones in variational quantum algorithms. *arXiv preprint arXiv:1906.00476*, 2019.

[91] Raphael Kaubruegger, Pietro Silvi, Christian Kokail, Rick van Bijnen, Ana Maria Rey, Jun Ye, Adam M Kaufman, and Peter Zoller. Variational spin-squeezing algorithms on programmable quantum sensors. *Phys. Rev. Lett.*, 123(26):260505, 2019.

[92] Bela Bauer, Dave Wecker, Andrew J. Millis, Matthew B. Hastings, and Matthias Troyer. Hybrid quantum-classical approach to correlated materials. *Phys. Rev. X*, 6:031045, Sep 2016.

[93] Alberto Peruzzo, Jarrod McClean, Peter Shadbolt, Man-Hong Yung, Xiao-Qi Zhou, Peter J Love, Alán Aspuru-Guzik, and Jeremy L O'Brien. A variational eigenvalue solver on a photonic quantum processor. *Nat Commun.*, 5:4213, 2014.

[94] M. Zwerger, H. Briegel, and W. Dür. Measurement-based quantum communication. *App. Phys. B*, 122:50, 06 2015.

[95] M Zwerger, HJ Briegel, and W Dür. Hybrid architecture for encoded measurement-based quantum computation. *Sci Rep*, 4(1):5364, 2014.

[96] M. Zwerger, H. J. Briegel, and W. Dür. Universal and optimal error thresholds for measurement-based entanglement purification. *Phys. Rev. Lett.*, 110:260503, Jun 2013.

[97] Nikolaj Moll, Panagiotis Barkoutsos, Lev S Bishop, Jerry M Chow, Andrew Cross, Daniel J Egger, Stefan Filipp, Andreas Fuhrer, Jay M Gambetta, Marc Ganzhorn, et al. Quantum optimization using variational algorithms on near-term quantum devices. *Quantum Sci. Technol.*, 3(3):030503, 2018.

[98] R. Hübener, C. Kruszynska, L. Hartmann, W. Dür, M. B. Plenio, and J. Eisert. Tensor network methods with graph enhancement. *Phys. Rev. B*, 84:125103, Sep 2011.

[99] Marc Hein, Jens Eisert, and Hans J Briegel. Multiparty entanglement in graph states. *Phys. Rev. A*, 69(6):062311, 2004.

[100] Marc Hein, Wolfgang Dür, Jens Eisert, Robert Raussendorf, M Nest, and H-J Briegel. Entanglement in graph states and its applications. *Proc. of the Int. School of Physics 'Enrico Fermi' on Quantum Computers, Algorithms and Chaos*, 2006.

[101] Scott Aaronson and Daniel Gottesman. Improved simulation of stabilizer circuits. *Phys. Rev. A*, 70:052328, Nov 2004.

[102] Maarten Van den Nest, Jeroen Dehaene, and Bart De Moor. Graphical description of the action of local clifford transformations on graph states. *Phys. Rev. A*, 69:022316, Feb 2004.

[103] A Yu Kitaev. Fault-tolerant quantum computation by anyons. *Ann. Phys.*, 303(1):2–30, 2003.

[104] W Dür, Gustavo Vidal, and J Cirac. Optimal conversion of nonlocal unitary operations. *Phys. Rev. Lett.*, 89:057901, 08 2002.

[105] N. Klco, E. F. Dumitrescu, A. J. McCaskey, T. D. Morris, R. C. Pooser, M. Sanz, E. Solano, P. Lougovski, and M. J. Savage. Quantum-classical computation of schwinger model dynamics using quantum computers. *Phys. Rev. A*, 98:032331, Sep 2018.

[106] C. J. Hamer, Zheng Weihong, and J. Oitmaa. Series expansions for the massive schwinger model in hamiltonian lattice theory. *Phys. Rev. D*, 56:55–67, Jul 1997.

[107] Esteban A Martinez, Christine A Muschik, Philipp Schindler, Daniel Nigg, Alexander Erhard, Markus Heyl, Philipp Hauke, Marcello Dalmonte, Thomas Monz, Peter Zoller, et al. Real-time dynamics of lattice gauge theories with a few-qubit quantum computer. *Nature*, 534(7608):516–519, 2016.

[108] Christine Muschik, Markus Heyl, Esteban Martinez, Thomas Monz, Philipp Schindler, Berit Vogell, Marcello Dalmonte, Philipp Hauke, Rainer Blatt, and Peter Zoller. U (1) wilson lattice gauge theories in digital quantum simulators. *New J. Phys.*, 19(10):103020, 2017.

[109] Frank Arute, Kunal Arya, Ryan Babbush, Dave Bacon, Joseph C Bardin, Rami Barends, Sergio Boixo, Michael Broughton, Bob B Buckley, David A Buell, et al. Hartree-fock on a superconducting qubit quantum computer. *Science*, 369(6507):1084–1089, 2020.

[110] Sidney Coleman. More about the massive schwinger model. *Ann. Phys.*, 101(1):239–267, 1976.

[111] Warit Asavanant, Yu Shiozawa, Shota Yokoyama, Baramee Charoensombutamon, Hiroki Emura, Rafael N Alexander, Shuntaro Takeda, Jun-ichi Yoshikawa, Nicolas C Menicucci, Hidehiro Yonezawa, et al. Generation of time-domain-multiplexed two-dimensional cluster state. *Science*, 366(6463):373–376, 2019.

[112] Mikkel V. Larsen, Xueshi Guo, Casper R. Breum, Jonas S. Neergaard-Nielsen, and Ulrik L. Andersen. Deterministic generation of a two-dimensional cluster state. *Science*, 366(6463):369–372, 2019.

[113] Konstantin Tiurev, Pol Llopart Mirambell, Mikkel Bloch Lauritzen, Martin Hayhurst Appel, Alexey Tiranov, Peter Lodahl, and Anders Søndberg Sørensen. Fidelity of time-bin entangled multi-photon states from a quantum emitter. *arXiv preprint arXiv:2007.09298*, 2020.

[114] Konstantin Tiurev, Martin Hayhurst Appel, Pol Llopart Mirambell, Mikkel Bloch Lauritzen, Alexey Tiranov, Peter Lodahl, and Anders Søndberg Sørensen. High-fidelity multi-photon-entangled cluster state with solid-state quantum emitters in photonic nanostructures. *arXiv preprint arXiv:2007.09295*, 2020.

[115] Ido Schwartz, Dan Cogan, Emma R Schmidgall, Yaroslav Don, Liron Gantz, Oded Kenneth, Netanel H Lindner, and David Gershoni. Deterministic generation of a cluster state of entangled photons. *Science*, 354(6311):434–437, 2016.

[116] T. Bastin, C. Thiel, J. von Zanthier, L. Lamata, E. Solano, and G. S. Agarwal. Operational determination of multiqubit entanglement classes via tuning of local operations. *Phys. Rev. Lett.*, 102:053601, Feb 2009.

[117] Julian Schwinger. Gauge invariance and mass. ii. *Phys. Rev.*, 128:2425–2429, Dec 1962.

[118] Cornelius Hempel, Christine Maier, Jonathan Romero, Jarrod McClean, Thomas Monz, Heng Shen, Petar Jurcevic, Ben P. Lanyon, Peter Love, Ryan Babbush, Alán Aspuru-Guzik, Rainer Blatt, and Christian F. Roos. Quantum chemistry calculations on a trapped-ion quantum simulator. *Phys. Rev. X*, 8:031022, Jul 2018.

[119] Vincent E Elfving, Benno W Broer, Mark Webber, Jacob Gavartin, Mathew D Halls, K Patrick Lorton, and A Bochevarov. How will quantum computers provide an industrially relevant computational advantage in quantum chemistry? *arXiv preprint arXiv:2009.12472*, 2020.

[120] Natalie Klco, Martin J Savage, and Jesse R Stryker. Su (2) non-abelian gauge field theory in one dimension on digital quantum computers. *Phys. Rev. D*, 101(7):074512, 2020.

[121] Bobak T Kiani, Giacomo De Palma, Dirk Englund, William Kaminsky, Milad Marvian, and Seth Lloyd. Quantum advantage for differential equation analysis. *arXiv preprint arXiv:2010.15776*, 2020.

[122] Alexander B. Zamolodchikov and Alexei B. Zamolodchikov. Factorized s Matrices in Two-Dimensions as the Exact Solutions of Certain Relativistic Quantum Field Models. *Annals Phys.*, 120:253–291, 1979.

[123] Alberto Peruzzo, Jarrod McClean, Peter Shadbolt, Man-Hong Yung, Xiao-Qi Zhou, Peter J. Love, Alán Aspuru-Guzik, and Jeremy L. O'Brien. A variational eigenvalue solver on a photonic quantum processor. *Nat. Commun.*, 5:1, 2014.

APPENDICES

Appendix A

Introduction to VQEs

The purpose of this appendix is to summarize how the variational quantum eigensolver (VQE) algorithm works; more details can be found in Ref. [7, 8, 123]. In this paper, the goal of the VQE is to approximate the lowest eigenvalue and corresponding eigenstate of the considered target Hamiltonian $\hat{H}_T$. This is accomplished by using a closed feedback loop between the quantum processor and a classical optimizer.

The algorithm is as follows. First, the initial state $|\psi_{\text{in}}\rangle$ is prepared on the quantum hardware. A good initial state is one which can be easily prepared on the quantum platform with high fidelity. Next, a sequence of gates is applied to the initial state. The gates in this sequence are the unitaries $\exp(-i\theta_k \hat{H}_R^{(j)})$, where $\hat{H}_R^{(j)}$ are the available resource Hamiltonians. Note that the set of available interactions does not need to be a universal gate set; a restricted gate set specific to the target Hamiltonian or the problem at hand is sufficient. The θ_k are the variational parameters; they are controlled by the classical optimizer and passed to the quantum device. In the circuit, the θ_k manifest as the product of the interaction strength of $\hat{H}_R^{(j)}$ and the time for which the gate is applied. In a typical VQE circuit a certain sequence of gates is often repeated with different variational parameters, each elementary sequence of gates that is repeated is called a layer.

Once the VQE circuit has been applied to the initial state, the result is the VQE ansatz state $|\Psi(\vec{\theta})\rangle$. For example, if the circuit employs r resource Hamiltonians in each layer and L layers in the circuit, then

$$|\Psi(\vec{\theta})\rangle = \prod_{\ell=1}^{L} \prod_{j=1}^{r} \exp\left(-i\theta_{j+r(\ell-1)} \hat{H}_R^{(j)}\right) |\psi_{\text{in}}\rangle. \tag{A.1}$$

This ansatz state is supposed to approximate the ground state of $\hat{H}_T$, and the higher the number of layers in the circuit, the more tunable it is. Eq. (A.1) gives a compact recipe for preparing a highly entangled state. Once the ansatz state is prepared for a given set of variational parameters, the cost function $\langle \Psi(\vec{\theta})|\hat{H}_T|\Psi(\vec{\theta})\rangle$ is evaluated on the quantum device. Since quantum measurements are an intrinsically stochastic process, the preparation and measurement of $|\Psi(\vec{\theta})\rangle$ needs to be repeated in order to have the correct expectation value with high accuracy. In particular, if the state is measured M times and σ_H^2 is the intrinsic variance of the target Hamiltonian, then the variance of the cost function is σ_H^2/M. The value of the cost function is fed to the classical computer which employs an optimization algorithm to choose new values for the variational parameters, with the goal of minimizing the cost function. The new variational parameters are fed to the quantum device, where the process begins anew. This cycle is repeated until the convergence threshold for the classical optimizer is reached.

Appendix B

Higgs Mechanism and Phase Structure in the Absence of a Topological Term

In this appendix we briefly review the Brout-Englert-Higgs mechanism for the continuum model and discuss its implications for the phase structure. To this end let us start from the continuum Lagrangian

$$\mathcal{L} = (D_\mu\beta)^*(D_\mu\beta) - \frac{1}{4}F_{\mu\nu}F^{\mu\nu} - V(|\beta|) \tag{B.1}$$

where β is a classical complex scalar field, $D_\mu = \partial_\mu + igA_\mu$ the covariant derivative with the gauge field A_μ and the coupling strength g, $F_{\mu\nu} = \partial_\mu A_\nu - \partial_\nu A_\mu$ the field strength tensor and $V(|\beta|) = -m^2|\beta|^2 + \frac{\lambda}{2}|\beta|^4$ with $\lambda > 0$. The first term of the action describes the kinetic energy of the scalar field and the coupling to the gauge field, the second term the kinetic energy of the gauge field, and the potential $V(|\beta|)$ contains the mass term and the self-interaction of the scalar field. It is straightforward to see that the action in Eq. (B.1) is invariant under U(1) gauge transformations given by

$$\beta(x) \rightarrow e^{ig\alpha(x)}\beta(x), \qquad A_\mu(x) \rightarrow A_\mu - \partial_\mu\alpha(x)$$

where $\alpha(x)$ is a real, differentiable function.

To get an intuition about the physics of the model, it is instructive to derive a semi-classical picture. To this end, we assume that the potential term is dominant and in the

ground state the field β fluctuates only slightly around the vacuum expectation value β_0 minimizing the potential $V(|\beta|)$. Rewriting the potential as

$$V(|\beta|) = \frac{\lambda}{2}\left[\left(|\beta|^2 - \frac{2m^2}{\lambda}\right)^2 - \left(\frac{m^2}{\lambda}\right)^2\right]$$

we see that $V(|\beta|)$ is quadratic function of $|\beta|^2$ and we can easily read off the minimum. Taking into account that $|\beta|^2$ is a positive semi-definite quantity, we have to distinguish two cases depending on the sign of m^2. (i) For $m^2 \leq 0$ the potential is a parabola in $|\beta|^2$ (see also lower left inset of Fig. 2.2) with a unique minimum at $\beta_0 = 0$. For $\beta \approx 0$ Eq. (B.1) reduces to

$$\mathcal{L} \approx -\frac{1}{4}F_{\mu\nu}F^{\mu\nu}$$

which is nothing but a *pure gauge theory* describing a *massless photon* and showing *charge confinement* [56]. (ii) For $m^2 > 0$ the potential has the shape of a "Mexican hat" (see also Fig. 2.2 in the main text) with the minima forming a level set given by

$$|\varphi_0|^2 = \sqrt{\frac{m^2}{\lambda}} =: \frac{v}{\sqrt{2}}. \tag{B.2}$$

In the expression above, we have defined the quantity $v = \sqrt{2m^2/\lambda}$ for convenience. To account for quantum fluctuations around β_0, we parameterize the field using polar representation

$$\beta(x) = \frac{v + h(x)}{\sqrt{2}}e^{i\frac{\phi(x)}{v}}$$

where the real fields $h(x)$ and $\phi(x)$ describe the fluctuations of the length of the field in radial direction and the phase. Plugging this expression in Eq. (B.1) and looking only at the gauge part $\mathcal{L}_{\text{gauge}}$ of the resulting Lagrangian we find

$$\mathcal{L}_{\text{gauge}} = -\frac{1}{4}F_{\mu\nu}F^{\mu\nu} + \frac{1}{2}m_p^2 A_\mu A^\mu, \tag{B.3}$$

showing that the *photon is massive* with mass $m_p = gv$. Moreover, in that case the *U(1) symmetry is spontaneously broken* as the vacuum of the theory corresponds to a single one of the minima described by Eq. (B.2). Sending $\lambda \to \infty$ while keeping the ratio m^2/λ fixed, the radial fluctuations can be neglected and β has a fixed length of $v/\sqrt{2}$. This is known

as fixing the length of the Higgs field. Plugging this expression in Eq. (B.1) one finds the effective Lagrangian

$$\mathcal{L}_{\mathrm{eff}} = \frac{1}{2}\partial_\mu\phi\partial^\mu\phi + \frac{1}{2}m_p^2 A_\mu A^\mu + m_p^2 A_\mu \partial^\mu\phi - \frac{1}{4}F_{\mu\nu}F^{\mu\nu}. \tag{B.4}$$

From Eq. (B.4) one can derive the Hamiltonian in Eq. (2.5) as shown in Ref. [21].

The simple semiclassical picture above shows that the model has two distinct regions. In the Higgs region the U(1) symmetry of the theory is spontaneously broken and the photon acquires a mass. In contrast, the confining region corresponds to a pure gauge theory describing a massless photon and the U(1) symmetry is intact. Going beyond this simple semiclassical picture and solving the the lattice discretization of Eq. (B.1) numerically using MCMC methods one finds a that the intuition from the rather simple semiclassical picture also hold true more generally [46, 56] and one obtains the phase diagram shown in Fig. 2.2 in the main text.

Appendix C

Periodicity and Symmetries of the Higgs Hamiltonian

Here we briefly show that physics is periodic in ε_0 with period 1 and discuss the symmetries of the lattice Hamiltonian. For simplicity we work with the formulation in Eq. (2.5), in which the gauge field has not been integrated out yet.

To show that physics is periodic in ε_0, we consider the transformation

$$
\begin{aligned}
\hat{\phi}_n &\to \hat{\phi}_n^\dagger, \\
\hat{Q}_n &\to -\hat{Q}_n, \\
\hat{U}_n &\to \hat{U}_n^\dagger, \\
\hat{E}_n &\to -(\hat{E}_n + k), \quad k \in \mathbb{Z}.
\end{aligned}
\tag{C.1}
$$

Let us first focus on $k = 0$. In that case Eq. (C.1) corresponds to a charge conjugation transformation $\hat{\mathcal{C}}_n$ which exchanges particles and antiparticles. This transformation is unitary, and, in particular, we see that applying it twice we get the initial operators back, thus showing that $\hat{\mathcal{C}}_n^2 = 1$ and charge conjugation is a $\mathbb{Z}_2$ symmetry.

To get further insight into the case $k \neq 0$, we look at the commutation relation in Eq. (2.3), from which follows that the unitary operator $\hat{U}_n$ introduces integer shifts in $\hat{E}_n$:

$$
\hat{U}_n^\dagger \hat{E}_n \hat{U}_n = \hat{E}_n - 1, \qquad \hat{U}_n \hat{E}_n \hat{U}_n^\dagger = \hat{E}_n + 1.
$$

Hence, by combining charge conjugation with $\hat{U}_n$ to $\hat{U}_n^k \hat{\mathcal{C}}_n \, [(\hat{U}_n^\dagger)^k \hat{\mathcal{C}}_n]$, we obtain an additional shift in the electric field by k positive (negative) units. Since both $\hat{\mathcal{C}}_n$ and $\hat{U}_n$ are unitary,

Eq. (C.1) indeed describes a unitary transformation. Applying this unitary transformation to the Gauss Law in Eq. (2.10) and the Hamiltonian in Eq. (2.5), we see that all terms are invariant except for the electric field energy which transforms according to

$$\sum_n (\varepsilon_0 + \hat{E}_n)^2 \to \sum_n (\varepsilon_0 - \hat{E}_n - k)^2 = \sum_n (\hat{E}_n + k - \varepsilon_0)^2.$$

Looking at that equation, we make the following observations. (i) For any value of ε_0 we can find a k such that the Hamiltonian is mapped to a unitarily equivalent one with $k - \varepsilon_0 \in [0, 1)$. Consequently, physics is periodic in ε_0 with period 1, and we can restrict ourselves to $\varepsilon_0 \in [0, 1)$ without loss of generality. (ii) For $k = 0$, $\varepsilon_0 = 0$ and $k = 1$, $\varepsilon_0 = 1/2$ the transformation from Eq. (C.1) is a symmetry of the Hamiltonian. In particular, for $\varepsilon_0 = 1/2$ there are two field configurations yielding the same electric energy. Thus, for $R^2 \to 0$ the ground state of the Hamiltonian is double degenerate and has a $\mathbb{Z}_2$ symmetry. This symmetry is preserved for non-vanishing R^2 along the critical line, before it is eventually spontaneously broken upon reaching the critical value R_c^2.

Appendix D

Location of the First Phase Transition

In this appendix we derive Eq. (2.17) from Section 2.3.2. This formula gives the smallest, positive value of ε_0 where a phase transition occurs and the dominant term in the ground state after the phase transition. Assume that R^2 is small, so that the second term in Eq. (2.14) (the kinetic term) can be ignored. Then, the Hamiltonian (including the penalty term) becomes

$$
\begin{aligned}
\hat{H} = \sum_{n=1}^{N} &\left(\left(\frac{1}{2R^2} + \frac{N-n}{2\beta} + \ell \right) \hat{Q}_n + \frac{\varepsilon_0(N-n)}{\beta} \right) \hat{Q}_n \\
&+ \sum_{n=2}^{N} \sum_{j=1}^{n-1} \left(\frac{N-n}{\beta} + 2\ell \right) \hat{Q}_j \hat{Q}_n - \beta(N-1) + \frac{\varepsilon_0^2}{2\beta}(N-1).
\end{aligned}
\tag{D.1}
$$

Before the transition, ε_0 and R^2 are small, so we expect the ground state to be approximately $|0\rangle^{\otimes N}$ plus small corrections from the other basis states (see Section 2.3.2 for more details). In this approximation, we note that $\hat{H}|0\rangle^{\otimes N} = (N-1)(\frac{\varepsilon_0^2}{2\beta} - \beta)|0\rangle^{\otimes N}$. Since the ground state energy is a continuous function of ε_0, we expect $\hat{H}|\psi\rangle = (N-1)(\frac{\varepsilon_0^2}{2\beta} - \beta)|\psi\rangle$, where $|\psi\rangle$ is the ground state after the phase transition. From the form of Eq. (D.1), $|\psi\rangle$ must be a charge basis state and, as discussed in Section 2.2.1, it must also have zero total charge. Additionally, since $R^2 \ll 1$, the $\sum_n c_n \hat{Q}_n^2$ term in Eq. (D.1) strongly penalizes states with many non-zero charges. As a result, we expect the ground state after the phase transition to be of the form $|\psi\rangle = |0\rangle^{\otimes n_1-1}|k\rangle|0\rangle^{\otimes n_2-n_1-1}|-k\rangle|0\rangle^{\otimes N-n_2}$ with $n_2 > n_1$ and

$k \in \mathbb{Z}$, where the minimum allowed number of charges have been changed in order to remain in the zero total charge sector. Acting the Hamiltonian in Eq. (D.1) on this state gives an energy of

$$\frac{k^2}{R^2} + \frac{k^2 r}{2\beta} + \frac{k\varepsilon_0 r}{\beta} - \beta(N-1) + \frac{\varepsilon_0^2}{2\beta}(N-1),$$

where $r = n_2 - n_1$. Equating this expression to the energy before the transition gives

$$\varepsilon_0 = -k\left(\frac{1}{2} + \frac{\beta}{R^2 r}\right).$$

Since $\varepsilon_0 > 0$, that forces $k < 0$. So, for each value of k and r, this formula predicts where the first phase transition could occur. Of course, of all the possible choices of k and r, the one that predicts the smallest value for the phase transition point ε_0 will be the true formula. Since $k \neq 0$ (no phase transition would occur in that case), we therefore choose $k = -1$ and $r = N - 1$. Thus, we predict the first phase transition to cause the ground state to transform from $|0\rangle^{\otimes N}$ to $|-1\rangle|0\rangle^{\otimes N-2}|+1\rangle$ at the point

$$\varepsilon_0 = \frac{1}{2} + \frac{\beta}{R^2(N-1)}. \tag{D.2}$$

Appendix E

Generation of $\hat{H}_{\mathrm{NN}}$ Interaction in a Parametric Cavity

In this appendix, we describe how the interaction $\hat{H}_{\mathrm{NN}}$ from Eq. (2.25b), which is one of the resource Hamiltonians used in the VQE, can be generated on the microwave platform. The derivation is very similar to the one presented in Ref. [67]. Using a symmetric SQUID, the fourth order term in the SQUID cosine potential is

$$\hat{H}_{\mathrm{SQ}} = g_0 \left(\hat{a}_p + \hat{a}_p^\dagger \right) \left(\sum_{n=1}^{N} \hat{a}_n + \hat{a}_n^\dagger \right)^4,$$

where $\hat{a}_p$ ($\hat{a}_n$) is the annihilation operator for the pump mode (cavity mode n) and g_0 is the intrinsic interaction strength between the pump and the cavity modes. The higher order terms in the cosine potential are neglected. As a result, the full Hamiltonian of the flux-pumped regulator is

$$\hat{H} = \hat{H}_0 + \hat{H}_{\mathrm{SQ}},$$

$$\hat{H}_0 = \omega_p \hat{N}_p + \sum_{n=1}^{N} \omega_n \hat{N}_n,$$

where ω_p is the natural frequency of the pump and ω_n is the natural frequency of mode n. We then transform $\hat{H}$ and go to the interaction picture using the operator $\hat{U} = \exp(i\hat{H}_0' t)$, where $\hat{H}_0' = \omega_p \hat{N}_p + \sum_n \omega_n' \hat{N}_n$. The resulting Hamiltonian $\hat{H}_{\mathrm{int}}$ is

$$\hat{H}_{\mathrm{int}} = \sum_{n=1}^{N} (\omega_n - \omega_n') \hat{N}_n + g_0 \left(\hat{a}_p e^{-i\omega_p t} + \mathrm{H.C.} \right) \left(\sum_{n=1}^{N} \hat{a}_n e^{-i\omega_n' t} + \mathrm{H.C.} \right)^4. \tag{E.2}$$

The first term of $\hat{H}_{\text{int}}$ can be identified with the free rotation part of the unitary evolution given in Eq. (2.25a), with $\Omega_n = (\omega_n - \omega'_n)t$. Let us focus on the second term in Eq. (E.2) for the rest of the derivation. We choose the frequency of the pump ω_p to be very small, in particular such that it is much less than each ω'_n. With this choice, the only terms in Eq. (E.2) without time dependence will be the terms in the expansion of $(\sum_n \hat{a}_n \exp(-i\omega'_n t) + \text{H.C.})^4$ with zero frequency. There are two types of these terms: a product of $\{\hat{a}_i^\dagger, \hat{a}_i, \hat{a}_j^\dagger, \hat{a}_j\}$, and a product of $\{\hat{a}_i^\dagger, \hat{a}_i, \hat{a}_i^\dagger, \hat{a}_i\}$. Using combinatorics and the bosonic commutation relations, the first type of terms sum to

$$24 \sum_{n=2}^{N} \sum_{k=1}^{n-1} \hat{N}_k \hat{N}_n + 12(N-1) \sum_{n=1}^{N} \hat{N}_n + 3N(N-1) \tag{E.3}$$

and the second type of terms sum to

$$6 \sum_{n=1}^{N} \hat{N}_n^2 + 6 \sum_{n=1}^{N} \hat{N}_n + 3N. \tag{E.4}$$

Combining Eqs. (E.3, E.4) together gives Eq. (2.25b) [the constant term is ignored since it contributes an overall phase to Eq. (2.25a)]. Using the rotating wave approximation, the remaining terms in Eq. (E.2) will average to zero, which results in only Eq. (2.25b) remaining. Finally, we assume that the pump has a strong coherent tone such that we can apply the parametric approximation and substitute $\hat{a}_p$ with its classical amplitude $|\alpha| e^{i\phi}$. With this approximation the time evolution induced by $\hat{H}_{\text{int}}$ is exactly the one given in Eq. (2.25a) with $\theta = (2g_0 |\alpha| \cos\phi)t$.

Appendix F

Ideal Higgs VQE

In this appendix we perform a simulation of a VQE that we call an ideal VQE. In an ideal VQE, we simplify the problem by neglecting the noisy statistics of the cost function and using the exact expectation value $\langle \hat{H}_{\text{HOBM}} \rangle$. An ideal VQE can be considered as a limiting case of a realistic VQE (detailed in Section 2.6) in the limit $M \to \infty$, that is, in the limit where one can perform an infinite number of measurements to evaluate the cost function. As a result, the variance of the cost function goes to zero, and the exact average $\langle \psi_{\text{VQE}} | \hat{H}_{\text{HOBM}} | \psi_{\text{VQE}} \rangle$ is given to the classical optimizer. The purpose of performing this ideal simulation is to show the best possible results that our VQE protocol, outlined in Section 2.6.1, can produce.

The numerical results for the ideal VQE are shown in Fig. F.1. The EFD is plotted against ε_0, both for the ideal VQE state (red dots) and the exact diagonalization ground state (blue curve). We can see that for both values of R^2 there is a good agreement between the EFD obtained by VQE and by exact diagonalization. In particular for the smaller value of R^2 the ideal VQE captures the discontinuity of the EFD, which is a sign of the phase transition, and for the larger value of R^2 the VQE result follows a smoother behaviour. For the $R^2 = 0.3$ plot, the fidelity of the VQE state (compared of the exact diagonalization ground state) is above 0.95 for all points and for the $R^2 = 0.6$ plot, the fidelity is above 0.85 for most points, with a maximum fidelity of 0.92 for $\varepsilon_0 = 0.5$ and a minimum fidelity of 0.78 for $\varepsilon_0 = 1.0$. The excellent results in the EFD comparison are confirmed by good fidelities and prove that our VQE procedure works in principle and is able to capture the phase transition given a large enough measurement budget.
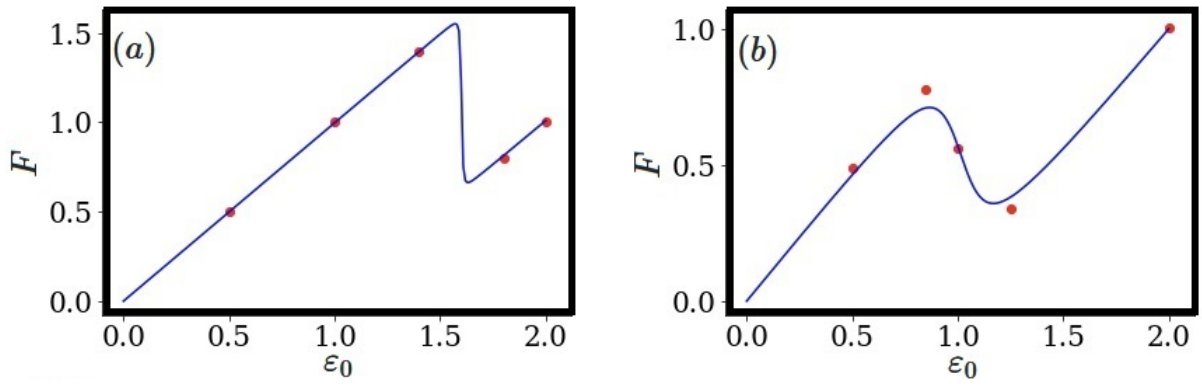
Figure F.1: **Ideal Higgs VQE results.** Electric field density F as a function of ε_0 for $\beta = 1.0$ and $R^3 = 0.3$ in *(a)* and $R^2 = 0.6$ in *(b)*. The blue line is the EFD of the exact diagonalization ground state and the red dots are the EFD of the VQE state. The beam splitter operations used in each block in the VQE are shown in Table 2.1.